

# Shell Model for Warm Rotating Nuclei

M. Matsuo, T. Døssing<sup>a</sup>, E. Vigezzi<sup>b</sup>, R.A. Broglia<sup>a,b</sup>, and K. Yoshida<sup>c</sup>

*Yukawa Institute for Theoretical Physics, Kyoto University, Kyoto 606-01, Japan*

<sup>a</sup> *Niels Bohr Institute, University of Copenhagen, Copenhagen Ø, DK2100, Denmark*

<sup>b</sup> *INFN sez. Milano, and Dept. of Physics, University of Milan, Milan, Italy*

<sup>c</sup> *Department of Physics, Kyoto University, Kyoto 606-01, Japan*

## Abstract

In order to provide a microscopic description of levels and E2 transitions in rapidly rotating nuclei with internal excitation energy up to a few MeV, use is made of a shell model which combines the cranked Nilsson mean-field and the residual surface delta two-body force. The damping of collective rotational motion is investigated in the case of a typical rare-earth nucleus, namely  $^{168}\text{Yb}$ . It is found that rotational damping sets in at around 0.8 MeV above the yrast line, and the levels which form rotational band structures are thus limited. We predict at a given rotational frequency existence of about 30 rotational bands of various lengths, in overall agreement with the experimental findings. The onset of the rotational damping proceeds quite gradually as a function of the internal excitation energy. The transition region extends up to around 2 MeV above yrast and it is characterized by the presence of scars of discrete rotational bands which extend over few spin values and stand out among the damped transitions, and by a two-component profile in the  $E_\gamma - E_\gamma$  correlation. The important role played by the high-multipole components of the two-body residual interaction is emphasized.

*PACS:* 21.10.Re, 21.10.-n, 23.20.Lv

*Keywords:* high spin states, rotational damping, cranked Nilsson potential, surface delta interaction.

## 1 Introduction

A heavy ion fusion reaction produces a hot and rapidly rotating compound nucleus. After emission of neutrons has cooled down the system, the compound nucleus still keeps high angular momenta (tens of  $\hbar$ ) and moderate heat energy, that is a moderate excitation energy (a few MeV) once the energy of rotational motion has been subtracted. It then emits a multitude of  $\gamma$ -rays, decreasing its spin and heat energy gradually, reaching finally the ground state.

For nuclei with mass number  $A \sim 170$  whose ground state has a stable elongated shape ( $\beta \sim 0.3$ ), up to around 20 different rotational bands have been observed in discrete gamma ray spectroscopy studies. The observed rotational bands lie in the lowest excitation energy region near the yrast line, representing the “cold” part of the whole of nuclear levels. In the excited region, say at 1 to 2 MeV above the yrast line, the level density at a given spin is as large as  $10^2$  to  $10^3$   $\text{MeV}^{-1}$  in normally deformed rare-earth nuclei. The equivalent level spacing of 10 to 1 keV is rather small in comparison to the typical size ( $\sim 10\text{keV}$ ) of matrix elements of the residual two-body nuclear force. The residual interaction then becomes effective to cause mixing of many-particle many-hole (or many-quasiparticle) configurations in the rotating deformed mean-field potential. Since different configurations respond differently to the Coriolis force due to different single-particle alignments, the

configuration mixing results in a dispersion of the rotational frequency within each energy eigenstate, implying a damping of the collective rotational motion [1, 2]. The gamma-rays which are emitted from the “warm” region (from about 1 MeV to about a few MeV above yrast, corresponding to temperature of a few hundred keV ) cannot be distinguished as discrete peaks and form a quasi-continuum in the spectra. Rotational damping has been studied experimentally through the analysis of the quasi-continuum spectra [3, 4, 5]. Recently, new experimental techniques have been devised to deal with the multi-dimensional quasi-continuum gamma-spectra obtained by double or triple coincidence gamma-ray experiments, making it possible to study in detail various aspects of the collective rotational motion in the warm region [6, 7, 8, 9, 10, 11]. In particular, the fluctuation analysis method [6, 7] has revealed that the number of rotational bands existing in a rare-earth nucleus is only around 30 at a given rotational frequency, thus confirming the occurrence of the rotational damping.

Early theoretical studies of the rotational damping dealt with the E2 strength function associated with the damped rotational motion, which is obtained by assuming that the configuration mixing is described by the general statistical theory of random matrices [1, 2, 12, 13]. In this paper we present a microscopic shell model able to describe individual nuclear levels and E2 transitions in the warm region, in order to study in more detail the transition from the regime of discrete rotational bands into the regime of damped rotational motion. Our description is based on a mean field calculated by the cranking model, which has been quite successful in the description of the low-lying portion of the nuclear spectrum (cf. e.g. [14, 15, 16, 17, 18]). We then add a two-body effective interaction, mixing the mean-field configurations. The first attempt along this line was made in Ref.[19], where a rather schematic residual interaction was employed in the calculations. We instead adopt somewhat more “realistic” effective nuclear force, i.e., the surface delta force [20]. We found in previous studies[21, 22] that the high-multipole components, which are present in this force, are essential to produce the rotational damping. In the present formulation, the emphasis is put not only on the residual two-body force but also on the construction of the diabatic single-particle basis, which enables us to describe long sequences of the rotational E2 transitions. To be noted is that both the particle-rotor model [23] and the interacting boson model [24] have been used to attack problems similar to the one we are dealing with in the present paper. Both of these models are more complete than the present one with respect to the angular momentum coupling in wave functions and E2 transition matrix elements. However, they are severely restricted by taking into account only a small part of many-particle many-hole excitations (single- $j$  orbits and  $s,d$ -bosons, respectively). The present approach includes all the excitations in the single-particle orbits in deformed nuclei within a given excitation energy.

After describing the formulation in Sect.2, we present numerical results for  $^{168}\text{Yb}$  in Sect.3. We investigate in detail the excited states in the warm region of the nuclear spectrum with very high spins as well as associated E2 transitions, which characterize the collective rotational motion. In particular, we look into the properties of rotational damping and compare them with available experimental data. In Sect.4, we study in detail high multipole components of the two-body effective force and compare the surface delta interaction with the pairing plus quadrupole-quadrupole force.

## 2 Formulation

### 2.1 Single-particle basis

We consider deformed nuclei with stable prolate shape. In such a nucleus, rotational bands observed by the discrete gamma-spectroscopy are often interpreted in terms of the single-particle excitations in cranked mean-field models where the collective rotational excitation is described in a semi-classical way while the intrinsic particle excitations are described quantum mechanically. For example, the cranked Nilsson model is widely used and gives a realistic description of the single-particle excitation modes in the high spin yrast region [17, 18]. Let us assume that the potential surface at a given spin displays a deep minimum in the space of the deformation parameters for a prolate deformation. In such a case, it should be possible to have intrinsic excitations of many particles and holes (or many quasiparticles) on top of the stable deformed mean field state. The excited states above the yrast

line are to be built out of these excited configurations.

In keeping with this picture, we formulate a shell model in which the single-particle basis is represented by the cranked Nilsson model and the many-particle many-hole ( $np$ - $nh$ ) excitations associated with the single-particle potential are taken into account to represent the intrinsic excitations in rotating nuclei. The collective E2 transitions are assumed to keep the intrinsic structure, that is, each of the  $np$ - $nh$  configurations forms a rotational band. Since the level density of the  $np$ - $nh$  states is high, the residual two-body force causes mixing among the  $np$ - $nh$  excitations, that is, mixing among the rotational bands. The configuration mixing can be taken into account explicitly by solving a shell model Hamiltonian which combines the cranked Nilsson mean-field and the residual two-body force

In the following, we describe the details of the model. Let us start with the single-particle basis. The single-particle Hamiltonian in the present theory is given by the cranked Nilsson model

$$h_{crank} = h_{Nilsson} - \omega j_x, \quad (1)$$

in which the protons and neutrons move in a deformed Nilsson potential which rotates around the axis with the largest moment of inertia (taken conventionally as the  $x$  axis), with uniform rotational frequency  $\omega$ . We shall not include the pairing potential in the mean-field Hamiltonian. Note, however, that pairing correlations may be partly taken into account through the configuration mixing caused by the residual interaction. Moreover, we shall be mainly interested in levels at very high spins  $I \gtrsim 30$ , where the pairing gap is expected either to be small or to vanish, due to the Coriolis anti-pairing effect [25, 26, 27]. Inclusion of the pairing potential in  $h_{crank}$  may improve the description of near-yrast rotational bands at low spins. However, use of the quasiparticle scheme may lead to incorrect description of highly excited states since many-quasiparticle configurations accompany spurious components related to the nucleon number violation. We use the Nilsson potential [28] with a single-stretched  $l^2$  term and an  $ls$  force whose parameters are given in [18]. The quadrupole and hexadecapole deformation parameters of the Nilsson potential ( $\epsilon, \epsilon_4$ ) should in principle be determined selfconsistently by minimizing the potential energy surface. The numerical calculations presented in the present paper were carried out with the deformation parameters  $(\epsilon, \epsilon_4) = (0.255, 0.014)$  for  $^{168}\text{Yb}$ , according to Ref.[29]. The single-particle basis keeps the signature and parity quantum numbers.

The eigenstates of the cranked Nilsson Hamiltonian, Eq.(1), define the adiabatic single-particle orbits. The eigenrouthians and the single-particle wave functions vary with the rotational frequency  $\omega$ . From time to time pairs of orbits cross each other as a function of  $\omega$  (See fig.1). If we magnify the crossing among the orbits with the same quantum numbers, it is seen that the two orbits “repel” each other. The nature of the two orbits interchanges across the crossing. This causes an abrupt change in the single-particle orbits as a function of the rotational frequency. This abrupt change makes it difficult to define the rotational bands on the basis of the single-particle orbits given adiabatically. To remedy this problem and guarantee the smooth change as a function of  $\omega$ , a *diabatic basis* for the single-particle orbits [30] is constructed in place of the adiabatic eigen solutions. The method of constructing the diabatic basis is described in the Appendix A. The resulting diabatic routhian spectrum  $\{e'_i(\omega)\}$  is also shown in Fig.1. In the following, we adopt the diabatic single-particle basis with routhians  $\{e'_i(\omega)\}$ , single-particle wave functions  $\{\psi_i(\omega)\}$  and the associated angular momentum expectation value  $\{j_{x,i}(\omega)\}$ .

## 2.2 Unperturbed rotational bands

Once the single-particle basis is defined, the shell model basis of the many-body system is obtained by filling  $N$  neutrons and  $Z$  protons in the diabatic cranked Nilsson orbits. Based on the configuration where all the orbits up to the Fermi surface are occupied, one can generate many-particle many-hole ( $np$ - $nh$ ) excitations, which form shell model basis states for the excited states above the yrast line. The basis configurations, labeled by  $\mu$ , at spin  $I$ <sup>1</sup> are given by

$$|\mu(I)\rangle = \prod_{\text{occupied } i \text{ in } \mu} a_i^\dagger |0\rangle \quad (2)$$

---

<sup>1</sup>In this paper, the spin is measured in units of  $\hbar$

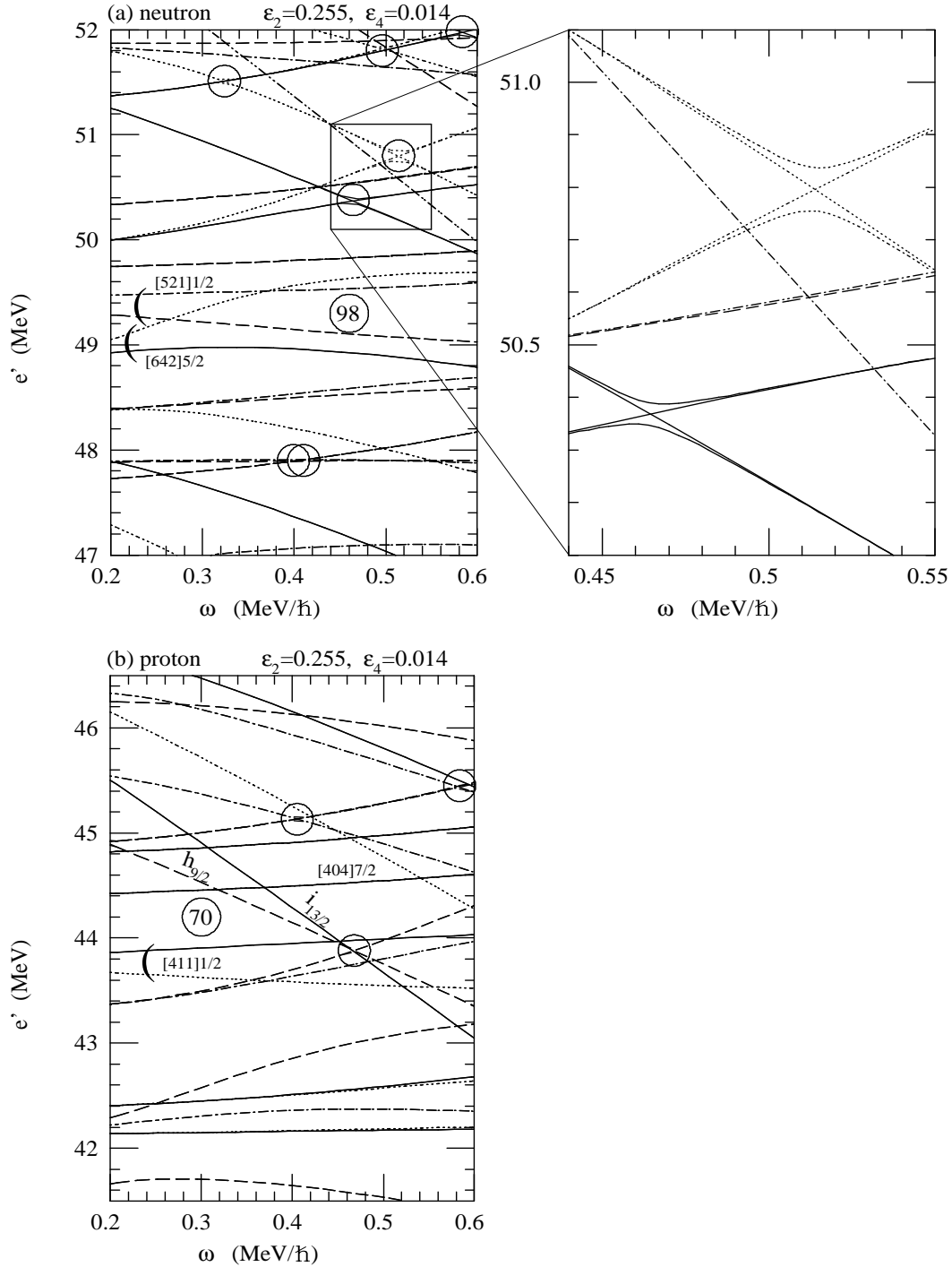


Figure 1: The cranked Nilsson single-particle routhian spectra for (a) neutrons and (b) protons with deformation parameter  $(\epsilon, \epsilon_4) = (0.255, 0.014)$ . The different kinds of curves denote different parity and signature;  $(\pi, \alpha) = (+, 1/2), (+, -1/2), (-, 1/2)$  and  $(-, -1/2)$  for solid, dotted, dashed and dot-dashed curves, respectively. The circles indicate the positions where the pair-wise repulsions take place. Both adiabatic and diabatic basis are plotted while they mostly overlay with each other. In the right panel, we show a magnified portion of the neutron routhian spectrum so that difference between the two basis becomes visible.

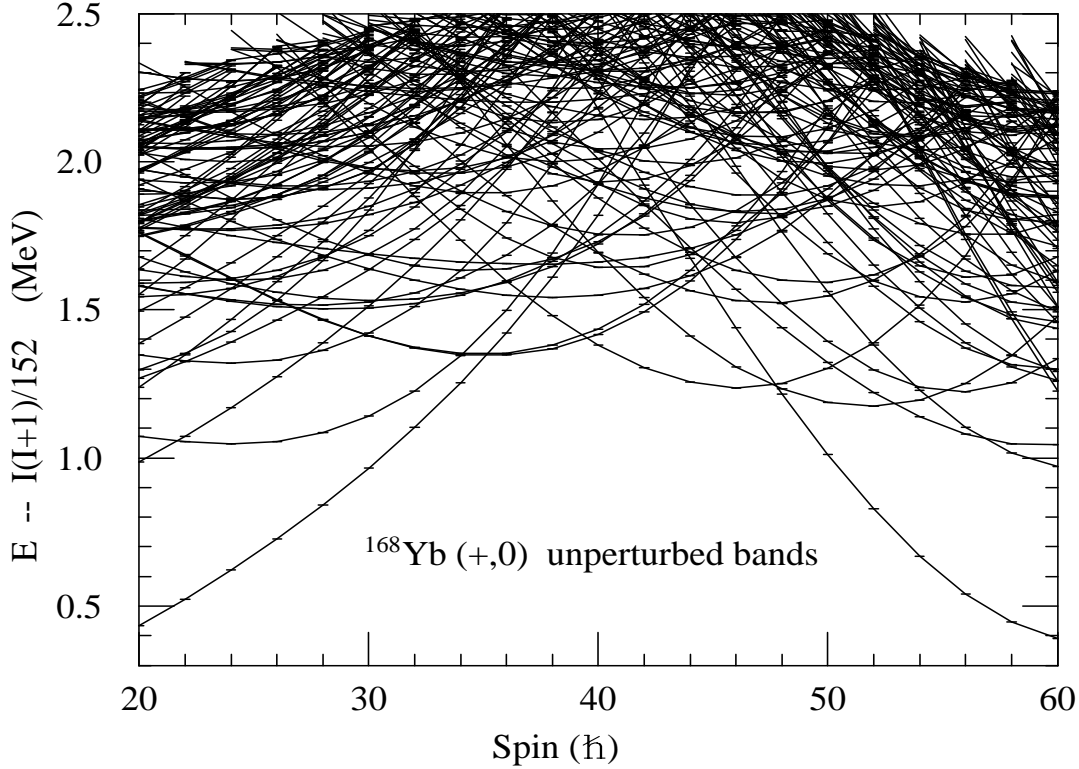


Figure 2: The unperturbed rotational bands in  $^{168}\text{Yb}$  with  $(\pi, \alpha) = (+, 0)$ . The lowest one hundred levels are plotted for each spin with small horizontal bars. A reference energy  $I(I + 1)/2J$  with  $J = 76 \text{ MeV}^{-1}$  is subtracted.

where  $a_i^\dagger$  represents the creation operator for the diabatic cranked Nilsson single-particle wave function  $\psi_i(\omega_I)$  occupied in this configuration. The rotational frequency  $\omega_I$  corresponding to the spin value  $I$  is calculated by imposing the condition

$$\langle J_x \rangle(\omega_I) = I \quad (3)$$

on the average value of the projection  $\langle J_x \rangle$  of the angular momentum on the rotation axis. Here this quantity is calculated by using thermal averaging as

$$\langle J_x \rangle = \sum_i j_{x,i}(\omega) f_i(\omega) \quad , \quad (4)$$

where  $j_{x,i}(\omega)$  is the expectation value of  $j_x$  of an orbit  $i$ , and  $f_i(\omega) = \{1 + \exp(e'_i(\omega) - \lambda)/T\}$  is the thermal occupation probability. The temperature parameter is chosen as  $T = 0.4 \text{ MeV}$  so that it corresponds to thermal excitation energy  $U \sim 2 \text{ MeV}$  relevant to the excited states under discussion.

The energy of the basis states in the laboratory frame is given by the Strutinsky renormalization method according to the prescription commonly used in the cranked Nilsson model [31, 32, 18]. Namely, the energy  $E_\mu(I)$  of the basis state  $\mu$  at spin  $I$  is given by

$$E_\mu(I) = E_\mu^{Nils}(I) - E^{smooth}(I) + E^{LD}(I) \quad (5)$$

Here the shell correction energy  $E_\mu^{Nils}(I) - E^{smooth}(I)$  is calculated microscopically with use of the diabatic single-particle basis. The bare energy  $E_\mu^{Nils}(I)$  is defined by  $E_\mu^{Nils}(I) = E'_\mu(\omega) + \omega J_{x,\mu}(\omega)$  with a constraint  $J_{x,\mu}(\omega) = I$  on the rotational frequency  $\omega$ . Here  $E'_\mu(\omega)$  and  $J_{x,\mu}(\omega)$  are the total routhian and the expectation value of the angular momentum  $J_x$ , respectively. Utilizing the diabatic single-particle routhian basis,  $E'_\mu(\omega)$  and  $J_{x,\mu}(\omega)$  change smoothly as a function of the rotational

frequency, and it is possible to approximate the bare energy  $E_\mu^{Nils}(I)$  in the laboratory frame as

$$E_\mu^{Nils}(I) = E'_\mu(\omega_I) + \omega_I I + \frac{(I - J_{x,\mu}(\omega_I))^2}{2J_\mu^{(2)}}, \quad (6)$$

$$E'_\mu(\omega_I) = \sum_{\text{occupied } i \text{ in } \mu} e'_i(\omega_I), \quad (7)$$

$$J_{x,\mu}(\omega_I) = \sum_{\text{occupied } i \text{ in } \mu} j_{x,i}(\omega_I), \quad (8)$$

$$J_\mu^{(2)} = \left. \frac{dJ_{x,\mu}}{d\omega} \right|_{\omega_I}, \quad (9)$$

by means of the second order extrapolation from the reference rotational frequency  $\omega_I$  [19, 33]. The deviation  $|J_{x,\mu}(\omega_I) - I|$  in the angular momentum expectation value is less than 5 at spin  $I = 50$  for most configurations in the present calculation. The Strutinsky smoothed energy is given by

$$E^{\text{smooth}}(I) = \sum_i e'_i(\tilde{\omega}) \tilde{n}_i + \tilde{\omega} I, \quad (10)$$

and

$$\tilde{J}_x(\tilde{\omega}) = \sum_i j_{x,i}(\tilde{\omega}) \tilde{n}_i = I, \quad (11)$$

with the smoothed occupation number  $\tilde{n}_i$  [34]. The rigid-body rotational energy  $E^{LD} = I(I + 1)/2J_{rigid}$  is calculated for the given shape of the potential ( $J_{rigid} = 80.3 \text{ MeV}^{-1}$  for  $^{168}\text{Yb}$ ). Since the single-particle orbits have good parity  $\pi$  and signature  $\alpha$ , the shell model basis states also conserve the same quantum numbers.

The energies  $\{E_\mu(I)\}$  and the many-body wave functions  $\{|\mu(I)\rangle\}$  define the shell model basis at a given spin  $I$  and parity  $\pi$ . It is assumed that to each  $np$ - $nh$  configuration there corresponds a rotational band. It is possible to make this correspondence uniquely and to follow the evolution of the band as a function of  $I$  in a continuous way because the basis states depend smoothly on the rotational frequency due to the diabatic construction of the single-particle basis. Such rotational bands are shown in Fig.2 for  $^{168}\text{Yb}$ .

### 2.3 Residual two-body interaction and shell model diagonalization

Since the mean-field potential is represented by the Nilsson deformed potential, it is the residual part of the two-body nuclear effective force that is to be taken into account as the shell model two-body interaction. In order to separate the residual part, we utilize the fact that, given a shell model configuration (a determinantal many-body state), any two-body force is decomposed unambiguously into the mean-field and the residual parts. The residual two-body interaction  $V_{\text{res}}$  associated with the reference shell model configuration, denoted by  $\mu_{\text{ref}}$ , is given by subtracting the mean-field part  $V_{\text{mf}}$  from the two-body interaction;

$$V_{\text{res}} = V_{2\text{body}} - V_{\text{mf}} + \langle V_{2\text{body}} \rangle. \quad (12)$$

Here the two-body interaction  $V_{2\text{body}}$  is expressed as

$$V_{2\text{body}} = \frac{1}{4} \sum_{ijkl} v_{ijkl} a_i^\dagger a_j^\dagger a_l a_k \quad (13)$$

with  $v_{ijkl} = \langle \psi_i(1)\psi_j(2) - \psi_j(1)\psi_i(2) | v(1,2) | \psi_k(1)\psi_l(2) \rangle$  being the anti-symmetrized matrix elements of the two-body force for the single-particle orbits  $i, j, k$ , and  $l$ . The mean-field part  $V_{\text{mf}}$  and a constant expectation value  $\langle V_{2\text{body}} \rangle$  is given by

$$V_{\text{mf}} = \sum_{ij} v_{ij}^{\text{mf}} a_i^\dagger a_j, \quad v_{ij}^{\text{mf}} = \sum_{\text{occupied } k \text{ in } \mu_{\text{ref}}} v_{ikjk}, \quad (14)$$

$$\langle V_{2\text{body}} \rangle = \frac{1}{2} \sum_{\text{occupied } jk \text{ in } \mu_{\text{ref}}} v_{jkjk}. \quad (15)$$

In this way, we could construct the residual interaction so that it has no diagonal matrix elements for the reference configuration, i.e.  $\langle \mu_{\text{ref}} | V_{\text{res}} | \mu_{\text{ref}} \rangle = 0$ . In the case of an even-even nucleus, we select as the reference  $\mu_{\text{ref}}$  the configuration in which the single-particle routhian orbitals are filled up to the Fermi level at low rotational frequency. We then take the diabatic continuation of the same configuration to extend to higher rotational frequencies. The residual interaction thus determined is essentially independent on spin or rotational frequency.

As the effective two-body effective force, we adopt the surface delta interaction (SDI) [20] with standard strength  $V_0 = 27.5/A$  [35] (See the Appendix B for details). The SDI has been used widely in the shell model descriptions of nuclei in a wide mass range from light nuclei to deformed rare-earth. The delta force acting only at the nuclear surface displays essential features needed for describing low-lying excitations. Note that it contains the pairing force in the particle-particle channel as well as the multipole-multipole forces in the particle-hole channel. In a later section, we will investigate this two-body force by changing its force strength as well as by comparing it with other effective forces.

Given the residual two-body interaction, the shell model Hamiltonian for the basis states  $\{|\mu(I)\rangle\}$  at spin  $I$  is constructed as

$$H(I)_{\mu\mu'} = E_{\mu}(I)\delta_{\mu\mu'} + V(I)_{\mu\mu'} \quad (16)$$

where  $V(I)_{\mu\mu'} = \langle \mu(I) | V_{\text{res}} | \mu'(I) \rangle$  are the matrix elements of the residual two-body interaction.

The energy eigenstates of the shell model Hamiltonian are obtained by numerical diagonalization. The resultant eigenstates are admixture of the shell model basis states, that is, the unperturbed rotational bands  $\mu's$ ,

$$|\alpha(I)\rangle = \sum_{\mu} X_{\mu}^{\alpha}(I) |\mu(I)\rangle \quad (17)$$

In carrying out the diagonalization, truncation of the basis states is necessary. For that purpose we first truncate the single-particle routhian orbitals so that only those located within  $\delta E_{max}$  above and below the Fermi surfaces are treated as active orbits. In the numerical calculations presented below, we choose  $\delta E_{max} = 3$  MeV, which corresponds to 20-30 orbitals for protons and for neutrons. We then consider all the  $np$ - $nh$  configurations whose routhian excitation energy  $\delta E' = \sum_{particles} e'_i - \sum_{holes} e'_j$  lies within the interval  $\delta E_{max}$ . This generates about 2000-3000  $np$ - $nh$  configurations for each  $I^{\pi}$ , most of which have 1p1h to 4p4h character while there is only a little contribution of 5p5h under the energy cutoff. The dimension of the basis is still too large to carry out systematic numerical diagonalization. To avoid this difficulty, we calculate the energy  $\{E_{\mu}(I)\}$  of the basis states  $\{|\mu(I)\rangle\}$  as well as the diagonal contribution to the basis energy of the residual interaction  $V(I)_{\mu\mu}$  for each configuration. The basis configurations are sorted up according to the energy  $E_{\mu}(I) + V(I)_{\mu\mu}$  containing the diagonal residual interaction, and the lowest  $10^3$  basis states are included for the shell model diagonalization. The diagonalization is done separately for each  $I^{\pi}$ .

## 2.4 E2 transition strengths

Using the assumption  $I \simeq I_x$ , the electromagnetic transition matrix elements can be calculated within the cranking model [36]. In order to calculate the stretched E2 transitions, we neglect minor contributions of the non-collective E2 transitions so that only the E2 matrix elements connecting the same intrinsic configuration are taken into account. Assuming that the nuclear shape is stable and independent of the configuration, the E2 operator then becomes proportional to a constant quadrupole moment  $Q_0$ ;

$$M_{\mu I, \mu' I-2} = \langle \mu(I) | M(E2, \lambda = 2, \mu_x = 2) | \mu'(I-2) \rangle \quad (18)$$

$$= \sqrt{\frac{15}{128\pi}} Q_0 \delta_{\mu\mu'} \quad (19)$$

where  $\delta_{\mu\mu'} = 1$  if the configuration  $|\mu(I)\rangle$  is the diabatic continuation of  $|\mu'(I-2)\rangle$ , and  $\delta_{\mu\mu'} = 0$  for other configurations.

The stretched E2 transition probability among the energy eigen states  $\alpha$  at  $I$  and  $\alpha'$  at  $I-2$  is calculated as

$$B(E2, \alpha I \rightarrow \alpha' I-2) = \frac{15}{128\pi} Q_0^2 M_{\alpha I, \alpha' I-2}^2 \quad (20)$$

with amplitude

$$M_{\alpha I, \alpha' I-2} = \sum_{\mu} X_{\mu}^{\alpha}(I) X_{\mu}^{\alpha'}(I-2) . \quad (21)$$

Hereafter, we often use the normalized E2 strength

$$S_{\alpha I, \alpha' I-2} \equiv M_{\alpha I, \alpha' I-2}^2 , \quad (22)$$

which satisfies  $\sum_{\alpha'} S_{\alpha I, \alpha' I-2} = 1$ , for E2 decays from the level  $\alpha$  at  $I$ . The normalized strength for a given transition coincides with the normalized transition probability or the branching ratio for the decay from  $\alpha$  at  $I$  to  $\alpha'$  at  $I-2$ , neglecting the  $E_{\gamma}^5$  factor.

In the experiments, only strong transitions are observed as discrete peaks in the gamma-ray spectra and the rest of the transitions shows up as quasi-continuum spectra which contain transitions summed over many states. For such situation, it is useful to represent the E2 transition properties by means of the distribution function of the strength, or the strength function. The strength function for the stretched E2 decay from the levels at  $I$  to the levels at  $I-2$  is given by

$$S_1(E_{\gamma}) = \sum_{\alpha \alpha'} S_{\alpha I, \alpha' I-2} f_{\alpha I} \delta(E_{\gamma} - E_{\alpha I} + E_{\alpha' I-2}), \quad (23)$$

where  $f_{\alpha I}$  is the feeding probability of the level  $\alpha$  at  $I$ . It becomes sometimes useful to define a strength function

$$S_{1, \alpha}(E_{\gamma}) = \sum_{\alpha'} S_{\alpha I, \alpha' I-2} \delta(E_{\gamma} - E_{\alpha I} + E_{\alpha' I-2}), \quad (24)$$

for stretched E2 gamma-decays from a given specific level  $\alpha$  at  $I$ . Average of  $S_{1, \alpha}$  weighted with the feeding probability is equivalent to the strength function defined by Eq.(23).

## 3 Results for $^{168}\text{Yb}$

### 3.1 Mixing of $np$ - $nh$ configurations

The calculations presented below were carried out for the deformed rare-earth nucleus  $^{168}\text{Yb}$ . For this nucleus there exist experimental data from the analysis of quasi-continuum gamma-spectra as well as data from discrete-peak spectroscopy identifying the rotational bands up to around  $I \sim 40$  [37, 38]. The potential energy surface in this nucleus has a stable minimum at prolate deformation  $\epsilon \sim 0.25$  up to  $I \sim 60$  [39, 18, 31], and many of the observed rotational bands are described as independent particle excitations in the cranked mean-field [38, 18]. This validates the basis assumption of the present model. We have also made calculations for other nuclei near  $^{168}\text{Yb}$  obtaining similar results.

The shell model diagonalization is done separately at each  $I^{\pi}$  for  $I = 20 - 61$ . The energies of the levels calculated within the lowest  $10^3$  basis states cover an interval of  $\sim 3$  MeV. The level density of these states is plotted in Fig.3 for a few spins as a function of the excitation energy  $U$  measured from the lowest state for a given  $I^{\pi}$ . It is compared with the Fermi gas level density with fixed signature and parity, appropriate for the cranked mean field [33],

$$\rho_{FG}(U) = \frac{\sqrt{\pi}}{48} a^{-\frac{1}{4}} U^{-\frac{5}{4}} \exp 2\sqrt{aU} \quad (25)$$

where  $a$  is the level density parameter. It is seen that the calculated level density increases exponentially as a function of the excitation energy, and follows approximately the Fermi gas formula up to about 2.5 MeV above the lowest state. The level density parameter fitting the calculated level density is about  $a \sim A/10$  MeV $^{-1}$ . This agrees with the standard estimate [40] based on the average single-particle level density in the harmonic oscillator model. The decrease of the level density at  $U \gtrsim 2.5$  MeV arises from the truncation of the basis states.

As a consequence of the configuration mixing caused by the residual interaction, the energy eigenstates  $\{|\alpha\rangle\}$  are admixture of many unperturbed states. In other words, the unperturbed states are spread over the energy eigenstates. The mixing is strongly dependent on the internal excitation



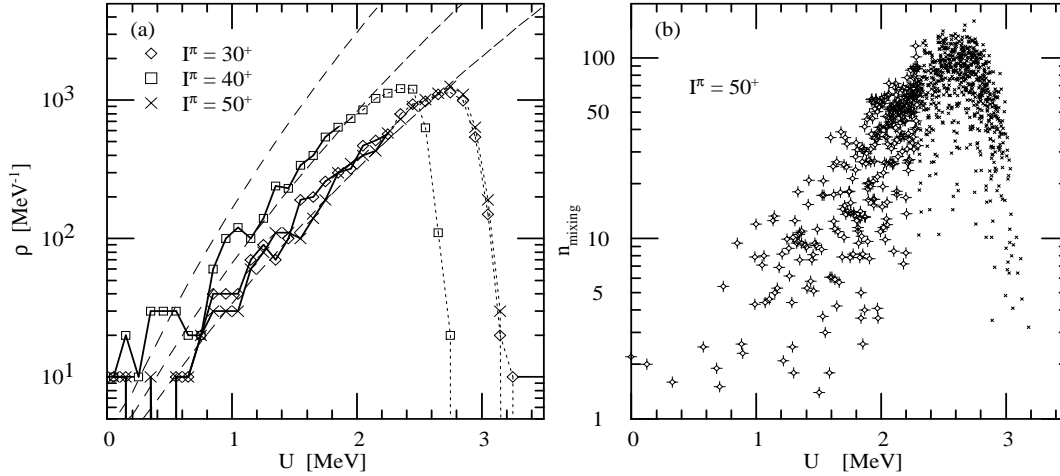


Figure 3: The level density for the calculated energy eigenstates with  $I^\pi = 30^+, 40^+, 50^+$  in  $^{168}\text{Yb}$  is plotted in the left panel as a function of the excitation energy measured from the lowest state with same  $I^\pi$ . The Fermi gas level density (long dashed lines) is also plotted with the level density parameter  $a = A/8, A/10, A/12$  MeV<sup>-1</sup>. The thick lines cover the energy region containing the lowest 300 levels while the short dashed lines continue above. In the right panel, the mixing number  $n_{\text{mixing}}$  is plotted for the calculated  $I^\pi = 50^+$  states. The lowest 300 states are labeled with a thick asterisk.

energy  $U$  of the states since the level density increases exponentially with  $U$ . A measure of the configuration mixing can be defined by means of a quantity

$$n_{\text{mixing}}(\alpha I) = \left( \sum_{\mu} |X_{\mu}^{\alpha}(I)|^4 \right)^{-1}, \quad (26)$$

which counts effectively the number of basis states  $\mu$ 's participating to form an energy eigenstate  $|\alpha\rangle = \sum_{\mu} X_{\mu}^{\alpha} |\mu\rangle$ . Note that, when all the states  $\mu$  have the same probability  $|X_{\mu}^{\alpha}|^2$ ,  $n_{\text{mixing}}$  gives the exact number of admixed states. This quantity, called the mixing number, is plotted in Fig.3(b) for a typical case at  $I^\pi = 50^+$  as a function of the excitation energy  $U$  measured from the yrast state. For the states near the yrast ( $U \lesssim 1$  MeV), the mixing number is less than about 3, which indicates that each of these states is composed of a few dominant configurations. As  $U$  increases, the mixing number increases steeply. For the states at  $U \sim 2$  MeV, several tens of  $np$ - $nh$  configurations contribute to form an energy eigenstate having rather complex wave functions. It is also to be noticed that the mixing number fluctuates significantly state by state. There are several states with low mixing number  $n_{\text{mixing}} < 3$  even at  $U = 1.5 - 2$  MeV where most of the others are strongly mixed with  $n_{\text{mixing}} \sim 10$ .

The effect of the truncation is visible both in Fig.3(a) and (b) for the levels at  $U \gtrsim 2.5$  MeV. We find that the lowest 300 levels located at  $U \lesssim 2.3$  MeV are stable against the truncation as far as the level density and the gross features of the mixing number are concerned.

### 3.2 Onset of rotational damping

The calculated energy levels are plotted in Fig.4 with little horizontal bars for  $(+, 0)$  states (positive parity and even spin) in  $^{168}\text{Yb}$ . In this picture, a reference rotational energy is subtracted from the calculated energy so that the vertical axis represents roughly the internal excitation energy of the nucleus. The solid lines connecting the energy levels represents strong E2 transitions. We use the convention that the E2 decay is “strong” if the associated normalized strength satisfies  $S > 1/\sqrt{2} = 0.707$ . Weaker transitions with  $0.5 < S < 0.707$  are displayed with dashed lines. It is seen that the strong E2 transitions (solid lines) form sequences of levels which are aligned regularly along a parabola like curve. Such sequences of levels represent rotational band structures. Most of

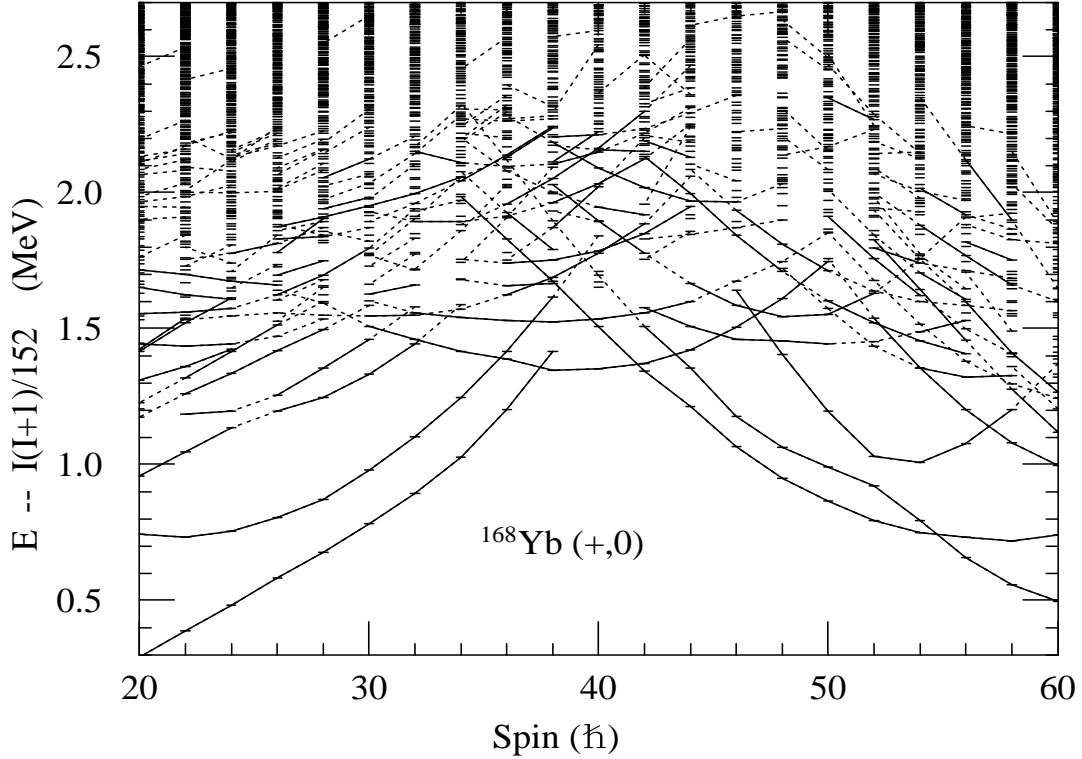


Figure 4: The calculated levels in  $^{168}\text{Yb}$  with  $(+,0)$  are shown with small horizontal bars. A reference energy  $I(I+1)/2J$  with  $J = 76 \text{ MeV}^{-1}$  is subtracted. The stretched E2 transitions which have the normalized strength  $S_{\alpha I, \alpha' I-2}$  larger than 0.707 are plotted with solid lines connecting initial and final levels of the transitions. Transitions with normalized strength between 0.5 and 0.707 are plotted with dashed lines.

the rotational bands lie in the region near the yrast, while the levels at higher excitations energy as a rule do not form band structures.

To indicate the E2 transition properties more precisely, we calculate distribution of the E2 transition strengths  $S_{1,\alpha}(E_\gamma)$ , Eq.(24), defined for gamma-decays from individual levels  $\alpha$  at  $I^\pi$ . They are shown in Fig.5 for the lowest levels with  $I^\pi = 30^+$ . The E2 strength associated with the first  $30^+$  level (which is the second lowest at spin 30) is concentrated in a single component feeding the  $28_1^+$  level with strength exhausting more than 95% of the total strength. The  $30_2^+$ ,  $30_3^+$  and  $30_4^+$  levels show essentially the same E2 distribution except slight difference in the gamma-ray energy for the dominant transition. The level  $30_5^+$ , with an internal excitation energy of about 700keV, displays a completely different E2 strength distribution, being fragmented over several transitions, each of which carries a rather weak strength. The E2 strength associated with the decay from the  $30_6^+$ ,  $30_7^+$ ,  $30_8^+$  and  $30_9^+$  levels shows a similar fragmentation. The fragmentation of the E2 strength increases as the excitation energy increases. Figure 6 displays the quantity  $S_{1,\alpha}(E_\gamma)$  associated with the levels  $30_{53}^+$  and  $30_{54}^+$  lying at  $U \sim 1.5 \text{ MeV}$  and for the levels  $30_{180}^+$  and  $30_{181}^+$  lying at  $U \sim 2.0 \text{ MeV}$ . At  $U \sim 1.5 \text{ MeV}$ , the E2 strength distribution has about ten branches, while the number of branches becomes much larger at  $U \sim 2.0 \text{ MeV}$ . The E2 strength is distributed within the range  $E_\gamma \sim 0.7 - 1.0 \text{ MeV}$ , with centroid at  $E_\gamma \sim 0.85 \text{ MeV}$  and with a width of about 150 keV.

The fragmentation of the E2 strength function is the rotational damping phenomenon [2]. Averaging the E2 strength distributions over many states (Fig.7) produces smooth profile for the strength distribution. The centroid of the distribution increases with the spin as expected from the relation  $\langle E_\gamma \rangle \sim 2\hbar\omega_{rot} \sim 2I/J$ ,  $J$  being the average moment of inertia. The width of the distribution is about 100 keV for  $I \sim 30$ , and 250 keV for  $I \sim 50$ . This approximately agrees with the estimate for the rotational damping width  $\Gamma_{rot} = 4\Delta\omega = 0.14(I/40)U^{1/4} \text{ MeV}$  in Ref.[2]. To be more precise, how-

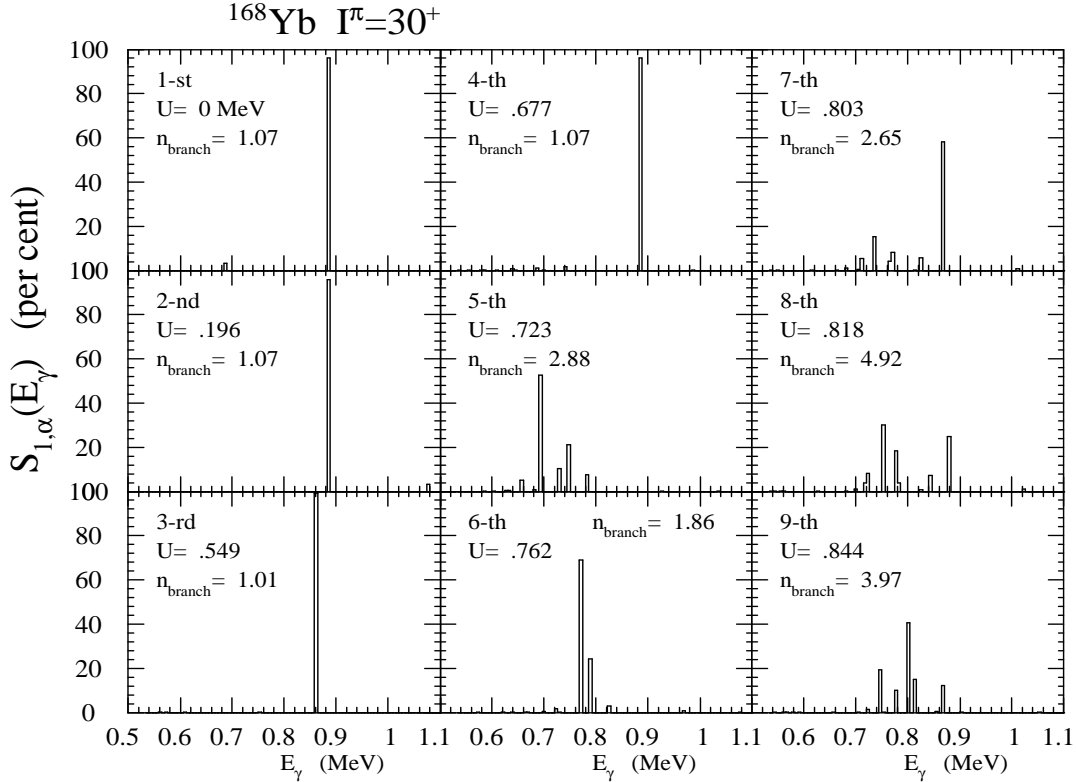


Figure 5: The distribution  $S_{1,\alpha}(E_\gamma)$  of the stretched collective E2 decays from the lowest 9 levels with  $I^\pi = 30^+$ . The branching number  $n_{branch}$  defined by Eq.(27) for the E2 decay and the relative excitation energy  $U$  (in unit of MeV) are put for each level. The bins for the transition gamma energy  $E_\gamma$  have a width of 6 keV.

ever, the strength distributions are not necessarily represented by a simple Lorentzian or Gaussian, but exhibit structures which reflect specific alignment properties of the underlying single-particle orbitals. In this particular nucleus, there exist two significantly aligned proton orbitals near the Fermi surface,  $\pi h_{9/2}$  and  $\pi i_{13/2}$  (see Fig.1). These aligned proton orbitals cross the  $Z = 70$  Fermi surface at  $\omega \sim 0.4$  MeV or  $I \sim 40$ . The peak at  $E_\gamma \sim 1.0$  MeV of the  $I = 40 \rightarrow 38$  strength distribution consists mainly of the transitions involving one of the aligned  $\pi h_{9/2}$  and  $\pi i_{13/2}$  orbitals while the little bump at  $E_\gamma \sim 1.2$  MeV arises from the components containing neither  $\pi h_{9/2}$  nor  $\pi i_{13/2}$ . An effect of the aligned proton orbits is also seen in Fig.4 as changes in slopes of the rotational band structures near the yrast at  $I \sim 40$  (see also the later discussion).

It may be useful to define the onset energy where the rotational damping sets in. In order to quantify the onset of rotational damping, let us utilize the branching number [43, 21, 22]

$$n_{branch}(\alpha) \equiv \left( \sum_{\beta} S_{\alpha I, \beta I-2}^2 \right)^{-1} \quad (27)$$

which counts effectively the number of the E2 branches for decays from a level  $\alpha$  at  $I$  to levels at  $I - 2$ . This quantity is analogous to the mixing number introduced in Eq.(26). Figures 5 and 6 also show the branching number for each level. As seen in Fig.5, the onset of damping can be characterized by a condition  $n_{branch} > 2$  implying an E2 decay with more than 2 branches. The dependence of the branching number with excitation energy is depicted in Fig.8. The branching number increases exponentially with internal excitation energy. With the criterion  $n_{branch} > 2$  for the onset of rotational damping, the onset energy is read from Fig.8 to be  $U \sim 800$  keV above yrast.

It should be emphasized that, although the onset energy thus defined tells approximately where the rotational damping sets in, the transition from the region of rotational bands to the region of

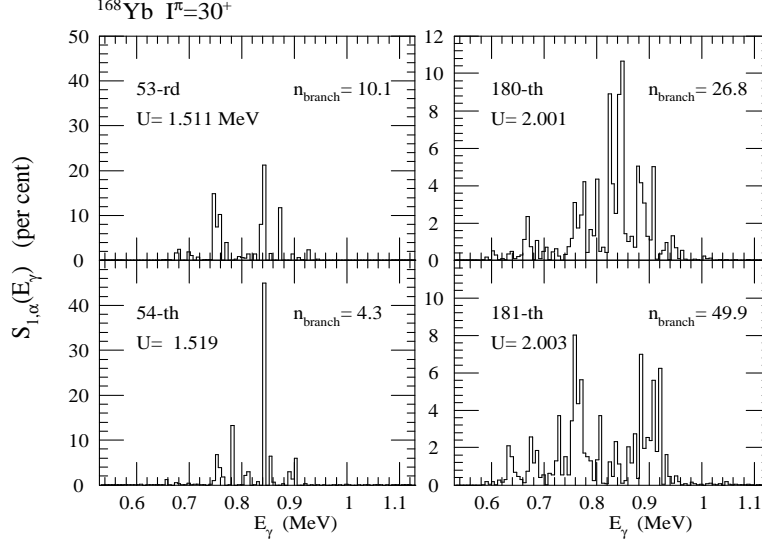


Figure 6: The strength distribution  $S_{1,\alpha}(E_\gamma)$  for the stretched collective E2 decays from the 53-rd, 54-th, 180-th, and 181-st excited levels with  $I^\pi = 30^+$ .

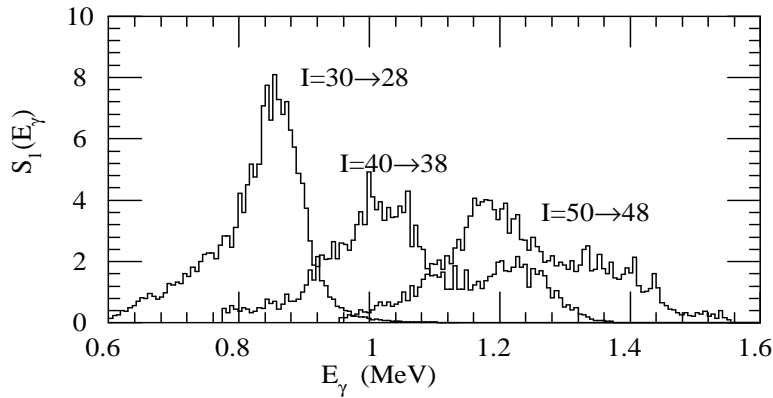


Figure 7: The strength function  $S_1(E_\gamma)$  for the E2 strength for the decays  $I = 30 \rightarrow 28$ ,  $I = 40 \rightarrow 38$  and  $I = 50 \rightarrow 48$ , summed over the lowest 200 states for both parities with a constant feeding probability  $f_{\alpha I}$ .

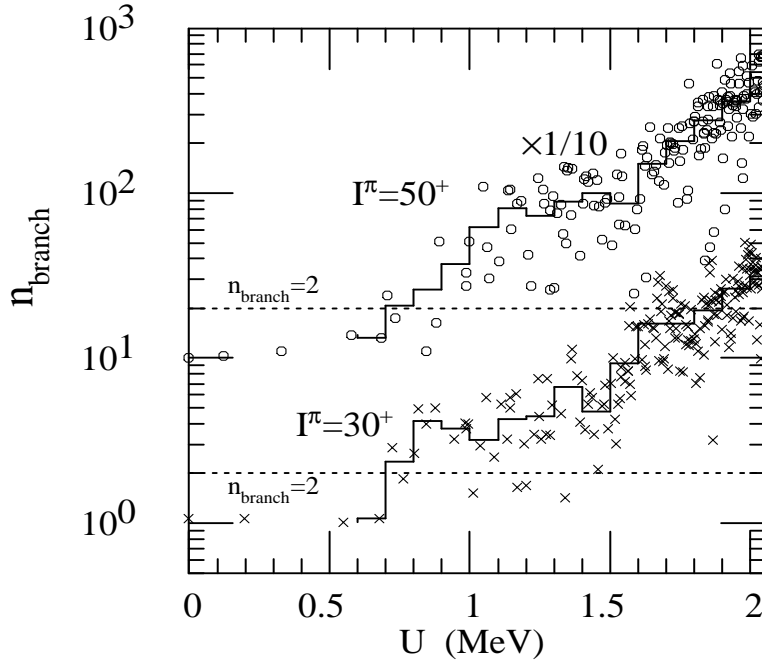


Figure 8: The E2 branching number  $n_{branch}$  for the  $I^\pi = 30^+$  (crosses),  $50^+$  states (circles) as a function of the excitation energy  $U$  of the states measured from the lowest one. The histogram shows  $n_{branch}$  averaged for energy bins.

rotational damping does not take place sharply at the onset energy, but rather develops gradually as the excitation energy increases. In fact, Fig.4 shows presence of many *short rotational bands* for which the strong E2 transitions (solid or dashed lines) continue for only a few to several steps. They lie from the border region  $U \sim 1$  MeV of the onset of rotational damping up to a region of much higher level density with  $U \sim 1.5$  MeV. Here the short band structures are surrounded by levels which do not have any strong transitions. This indicates that the rotational band structures partly remain even in the region of the rotational damping. Presence of such scars of rotational bands [41] is also displayed in Fig.8, from which it is seen that there exist levels whose branching number  $n_{branch}$  is smaller than 2 or 3 even at high excitation energy  $U \sim 1.5$  MeV. It is noticeable that the E2 strength distribution in the transition region is fluctuating quite irregularly from state to state as the Figs.6 and 8 indicates. Two panels in the left (right) hand side show quite different fine structures, even if they are produced from neighboring levels  $30_{53}^+$  and  $30_{54}^+$  ( $30_{180}^+$  and  $30_{181}^+$ ), corresponding to excitation energies which are the same within just 8 (2) keV.

### 3.3 Number of rotational bands

Since the rotational band structures do not survive in the region of high internal excitation energy, there exists only a finite number of discrete rotational bands in a single nucleus. This feature can be utilized to study experimentally the onset of rotational damping. Through the fluctuation analysis method [6, 7] it is possible to extract an effective number of gamma decay paths from the double-coincident  $E_\gamma \times E_\gamma$  spectrum. When this method is applied to the ridge structures in the spectrum, the effective number of paths essentially corresponds to the number of discrete rotational bands.

Let us define a corresponding quantity within the framework of the present calculation to be able to compare our results with the experimental findings. A straightforward definition is just to count the number of strong E2 transitions at a given spin with strength  $S$  larger than a given threshold  $S_{thr}$ , for which one may use  $S_{thr} = 1/\sqrt{2} = 0.707$  to define levels forming discrete rotational bands as adopted in plotting Fig.4. Keeping in mind the previous analysis for the onset of damping, another definition may also be used in terms of the branching number with criterion  $n_{branch} < 2$  for levels forming rotational bands. Note that these two criteria are not very different, since each state which

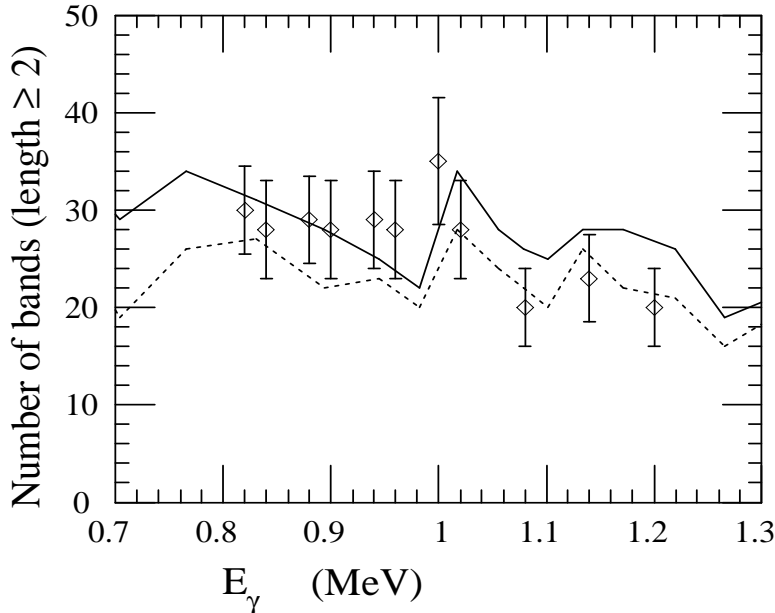


Figure 9: The calculated number of bands with length more than or equal to 2 is compared with the experimental effective number of paths [7] extracted from the first ridge of  $(E_{\gamma_1}, E_{\gamma_2})$  spectra in  $^{168}\text{Yb}$ . The solid line is calculated with the criterion  $n_{branch} < 2$  while the dashed line is defined with  $S > 0.707$ . The horizontal axis denotes the average gamma-ray energy  $E_\gamma = (E_{\gamma_1} + E_{\gamma_2})/2$ .

has a very strong transition with  $S > 0.707$  necessarily has a branching number  $n_{branch} < 2$ . The fluctuation analysis method is often applied to the first ridge located within the interval  $E_{\gamma_1} - E_{\gamma_2} = \pm 4/J$  in the  $E_\gamma \times E_\gamma$  spectra ( $J$  being the moment of inertia), which is formed by two consecutive E2 gamma-rays. Correspondingly we count the number of rotational bands which satisfy the above criteria at least over two steps  $I + 2 \rightarrow I \rightarrow I - 2$  of E2 decays. In practice, we count all the states which satisfy  $n_{branch} < 2$  or  $S > 0.707$  for both decaying transitions and feeding ones, and sum the numbers from four sets of parity and signature  $I^\pi = I_0^+, I_0^-, (I_0 + 1)^+, (I_0 + 1)^-$  for a given representative spin  $I_0$ . The calculated number of bands can be plotted as a function of spin  $I_0$  or the average gamma ray energy  $E_\gamma = (E_{\gamma_1} + E_{\gamma_2})/2$ . Figure 9 shows the calculated number of bands using the two criteria and compares them with the experimental effective number of paths associated with the first ridge. The two criteria give essentially the same number of bands around 30. It is noticed that the theoretical calculations and the data agree quite well in all the  $\gamma$ -ray energy range  $E_\gamma \sim 0.8 - 1.2$  MeV corresponding to spins  $I \sim 28 - 48$ .

More accurate comparison between the theory and the experiments requires evaluation of the feeding probabilities. This is possible by making a simulation of the whole gamma decay cascades combining microscopically calculated levels and E2 transitions with statistical description of E1 decays since the present model can describe levels up to about 2 MeV above yrast line at high spins, where most of the gamma decay cascades of a warm rotating compound nucleus proceed. Such a microscopic simulation has been developed recently[42]. From the  $E_\gamma \times E_\gamma$  spectrum produced from the simulation, the effective number of paths is extracted in the same way as the experimental analysis. In this manner, we can make comparison which does not depend on the particular choice of the threshold for  $S_{thr}$  or  $n_{branch}$  used for the definition of the number of bands. It is found that the effective numbers of paths both in the simulation and in the experiments for  $^{168}\text{Yb}$  agree quite well [42].

As discussed above, the calculations predict the presence of scars of rotational bands, that is, the “short” rotational band structures connected by strong E2 transitions for only a few decay steps. It may be possible to check this feature in the experiments by looking into the second and higher order ridges in the  $E_\gamma \times E_\gamma$  spectra. As the two consecutive gamma-rays from a rotational band fall on the first ridge at  $E_{\gamma_1} - E_{\gamma_2} = 4/J$ , two gamma-rays of the first and last decay steps in  $n$  consecutive

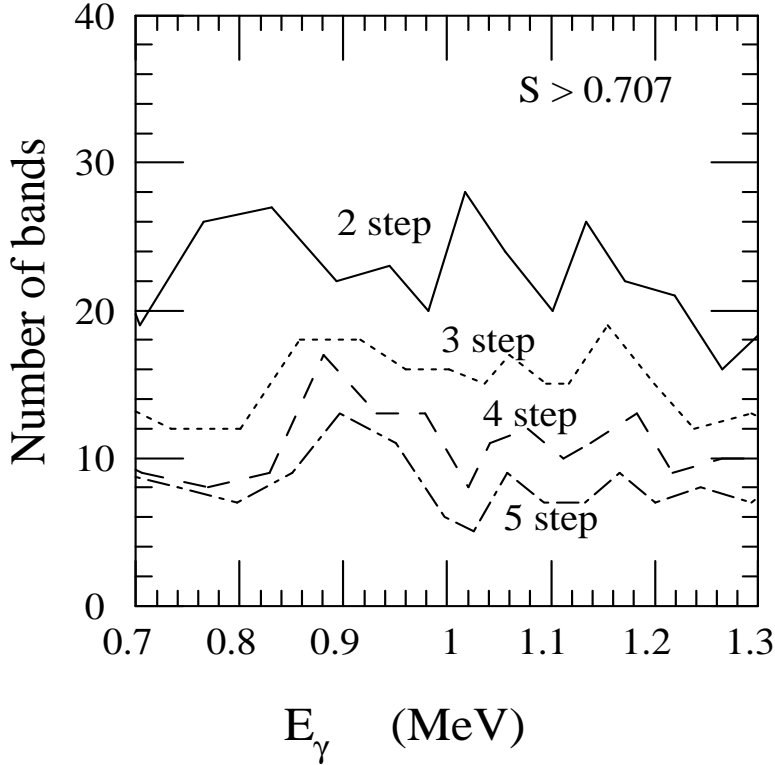


Figure 10: The calculated number of bands with length more than or equal to 2, 3, 4 and 5 steps, plotted with solid, dotted, and dot-dashed lines, respectively. In this figure, the criterion  $S > 0.707$  is used to define the rotational bands. The horizontal axis denotes the average gamma-ray energy  $E_\gamma = (E_{\gamma 1} + E_{\gamma 2})/2$ .

transitions should fall on the  $(n - 1)$ -th ridge at  $E_{\gamma 1} - E_{\gamma 2} = 4(n - 1)/J$ . Thus, for example, the effective number of path extracted from the second ridge tells the number of rotational band structures which continue for at least three consecutive steps. Since the rotational bands continuing only for two steps do not contribute to the second ridge, we may expect the effective number of paths for the second ridge to be smaller than that for the first ridge. This is illustrated in Figure 10. In this figure, we count the number of rotational bands defined by the criterion  $S > 0.707$  for various lengths of decay steps. In plotting the number of rotational bands, we used the average gamma-ray energy for the two gamma rays,  $I + 2 \rightarrow I$  and  $I - 2n + 2 \rightarrow I - 2n$ , for the rotational bands with  $\geq n$  decay steps. The calculation indicates that a considerable part of the first ridge comes from the scars of rotational bands at "high" heat energy. It also suggests that the effective number of path in the higher order ridges may be significantly smaller than in the first ridge. In fact, the experimental data for the higher order ridges also indicate this tendency [10]. In order to make a quantitative comparison, however, a more careful analysis using e.g., the microscopic simulation of Ref.[42] is required.

### 3.4 $E_\gamma - E_\gamma$ correlation

Since the quasi-continuum  $E_\gamma \times E_\gamma$  spectrum displays the characteristic ridge-valley structure, the shape of the spectrum provides us with important information about the rotational damping [9, 11]. The quasi-continuum analysis often deals with projection of the  $E_\gamma \times E_\gamma$  spectra upon the  $E_{\gamma 1} - E_{\gamma 2}$  axis. A quantity which is related to the projected spectra is the strength distribution function of the coincident two E2 transitions. In particular, the two-gamma strength function for consecutive E2 decays  $I + 2 \rightarrow I \rightarrow I - 2$  is important since it characterizes the shape of the first ridge as well as

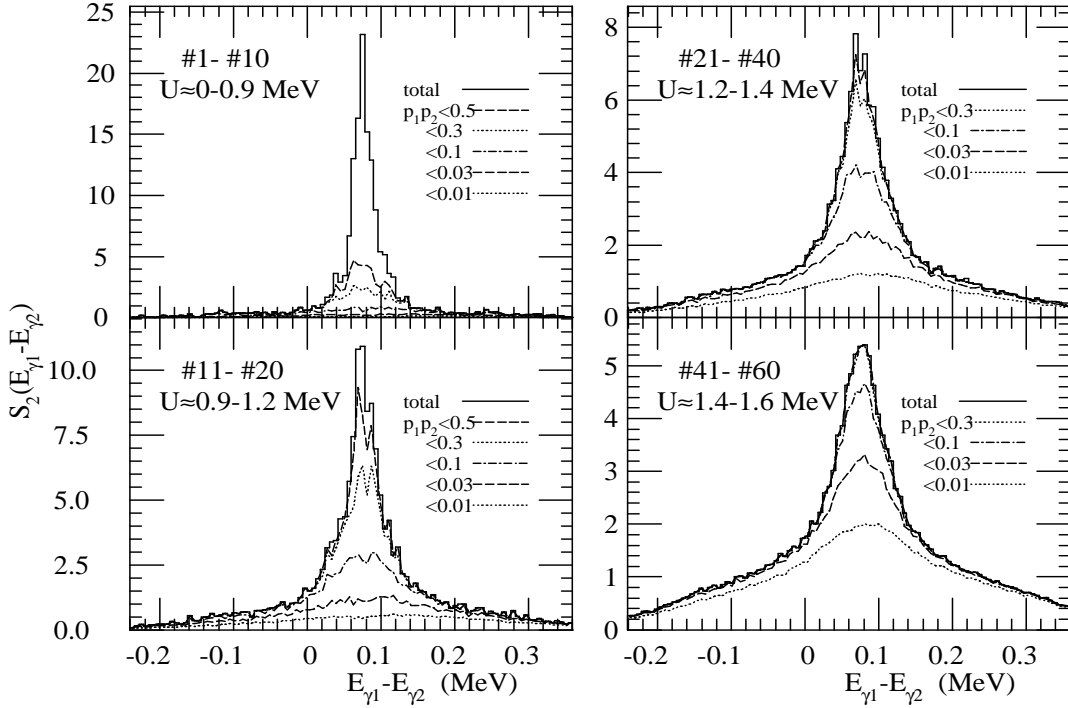


Figure 11: The two-step strength distribution  $S_2(E_{\gamma_1} - E_{\gamma_2})$  of consecutive E2 transitions for different bins of excited levels, defined for the lowest 10 levels, the 11-st to 20-th levels, the 21-st to 40-th, and 41-st to 60-th for each  $I^\pi$ . The strength is averaged for the spins  $I = 30 - 51$  in order to get enough statistics to produce smooth profile. The strength distribution is also subdivided with respect to the product strength  $p_1 p_2 = S_{\alpha I+2, \alpha' I} S_{\alpha' I, \alpha'' I-2}$  of individual transitions. The approximate excitation energy of the bin measured from yrast is put for each bin for the sake of reference.

of the central valley. The two-gamma strength function is given by

$$S_2(E_{\gamma_1} - E_{\gamma_2}) = \sum_{\alpha\alpha'\alpha''} S_{\alpha I+2, \alpha' I} S_{\alpha' I, \alpha'' I-2} f_{\alpha' I} \delta(E_{\gamma_1} - E_{\gamma_2} - E_{\gamma, \alpha \rightarrow \alpha'} + E_{\gamma, \alpha' \rightarrow \alpha''}) \quad (28)$$

where

$$E_{\gamma, \alpha \rightarrow \alpha'} = E_{\alpha I+2} - E_{\alpha' I} \quad (29)$$

$$E_{\gamma, \alpha' \rightarrow \alpha''} = E_{\alpha' I} - E_{\alpha'' I-2} \quad (30)$$

and the  $f_{\alpha I}$  is the feeding probability of the level  $\alpha$  at spin  $I$ .

The calculated two-gamma strength function  $S_2(E_{\gamma_1} - E_{\gamma_2})$  is depicted in Figure 11. Here an average is taken over the levels within a spin interval  $I = 30 - 51$ . In order to study the excitation energy dependence, the sum over  $\alpha'$  is divided into bins including 10 or 20 levels for each  $I^\pi$ . The feeding probability  $f_{\alpha' I}$  is put equal for all the levels. The lowest bin (#1-#10) covers approximately the energy region  $U = 0 - 0.9$  MeV, thus it mostly contains the E2 transitions associated with the rotational band structures near the yrast line. The higher bins cover the region above the onset of rotational damping.

For the lowest bin, the most characteristic feature is the presence of a sharp peak located at  $E_{\gamma_1} - E_{\gamma_2} \sim 70$  keV with a width of about 30 keV, which corresponds to the first ridge observed in the  $E_{\gamma} \times E_{\gamma}$  spectrum. In order to show the contents of the peak, the two-gamma strength function  $S_2(E_{\gamma_1} - E_{\gamma_2})$  is subdivided by putting cuts on the product strength  $S_{\alpha I+2, \alpha' I} S_{\alpha' I, \alpha'' I-2} \equiv p_1 p_2$  of each transition  $(\alpha, I+2) \rightarrow (\beta, I+2) \rightarrow (\gamma, I-2)$ . The sharp ridge in the lowest bin consists mostly of the strong transitions satisfying  $p_1 p_2 > 0.5$ . This indicates that the sharp ridge is formed by the



strong transitions ( $p > 1/\sqrt{2}$ ) associated with the rotational band structures. The peak position of the sharp ridge is related to an average dynamic moment of inertia  $J$  of these bands through  $E_{\gamma_1} - E_{\gamma_2} = 4/J$ , and the peak width originates from fluctuations in the moment of inertia among different bands.

For the higher bins (#11 – #20, #21 – #40, #41 – #60), the profile of the two-gamma strength function is quite different from that of the lowest bin in many respects. Note that there is only a little contribution of strong E2 transitions ( $p_1 p_2 > 0.5$ ) associated with the rotational band structure. This is because the rotational damping causes fragmentation of the E2 strengths with a spread in gamma ray energy of order of  $\Gamma_{rot}$ . Moreover, the spectrum shows a two component profile with wide and narrow widths of about 300 and 80 keV. The intensity of the wide component increases with the average energy of the bins. This component is easily understood as a consequence of the rotational damping. If two consecutive transitions were uncorrelated, the two-gamma strength function  $S_2(E_{\gamma_1} - E_{\gamma_2})$  would simply become a convolution of two single-gamma strength functions  $S_1(E_\gamma)$  for the consecutive steps, producing a smooth distribution with a width a factor of 2 larger (assuming a Lorentzian shape) than that of the single-gamma strength function  $S_1(E_\gamma)$ , which displays a width of about 100-200 keV (see Fig.7).

The narrow component has a width of about 80 keV, whose intensity decreases with the energy of the bin. The origin of the narrow component is visible in Fig.11 by subdividing the strength function with respect to the product strength  $p_1 p_2$  of individual transitions. It is noticed that the transitions building up the narrow component have *relatively* large strength compared to those composing the wide components. Taking the third bin (#21 – #40) as an example, the narrow component consists of transitions with  $0.03 < p_1 p_2 < 0.3$  while weaker transitions  $p_1 p_2 < 0.03$  contribute only to the wide component. These transitions in the narrow component are much stronger than the average strength ( $p_1 p_2 \sim (\Gamma_{rot} \rho)^{-2} \sim 0.01$ ) expected for damped transitions.

This analysis indicates that the correlation  $E_{\gamma_1} - E_{\gamma_2} \sim 4/J$  associated with the rotational band structure still remains in the consecutive E2 transitions even after the rotational damping sets in and that the narrow component has the same origin as the “scars” of the rotational bands discussed above. This suggests that the width of the narrow component is related to the spreading width which represents the extent of the configuration mixing of the rotational band structures.

It is also noticed that the narrow component is intense even at the fourth bin (#41 – #60) corresponding to excitation energy  $U \sim 1.5$  MeV above yrast. It becomes less intense as the excitation energy increases, and almost disappears at  $U \gtrsim 2$  MeV as shown in Fig.12. The development of rotational damping is quite gradual as a function of  $U$ , and the transition region extends from  $U \sim 0.8$  MeV to  $U \sim 2$  MeV above yrast line. Interestingly, it is found from the statistical analysis of energy level spacing and individual E2 strength [21, 22, 43] that the E2 strength shows the Porter-Thomas distribution at  $U \gtrsim 2$  MeV while it deviates significantly from the random limit for  $U \lesssim 2$  MeV. The deviation from the Porter-Thomas distribution and the presence of the narrow component are related with each other since both originate from the presence of strong transitions in the region of the rotational damping.

The  $E_{\gamma_1} - E_{\gamma_2}$  correlation only displays a weak dependence on angular momentum, as shown in Figure 13. The intensity of the narrow component becomes larger for lower spins although there exist significant narrow components even at very high spin ( $I \gtrsim 50$ ). The smaller the spin is, the smaller becomes the rotational damping width (width of the wide component). When the damping width becomes smaller, the branching number and strength of the fragmented E2 transitions becomes smaller and larger, respectively. Thus strong transitions which cause the narrow components become more dominant at lower spins. On the other hand, the width of the narrow component is not very dependent on spin. This also suggests that the narrow width may be related to the spreading width, which is essentially spin independent in the present model.

In the experiments, the actual  $E_{\gamma_1} \times E_{\gamma_2}$  spectrum is not simply represented by the two-gamma strength function discussed above since it is formed not only by the consecutive E2 transitions but also by non-consecutive E2's as well as E1 transitions all weighted by the feeding probability. It is found, however, by means of the simulation analysis [42] that the two-component profile causes significant effects on the spectral shape of the  $E_{\gamma_1} \times E_{\gamma_2}$  spectra [11].

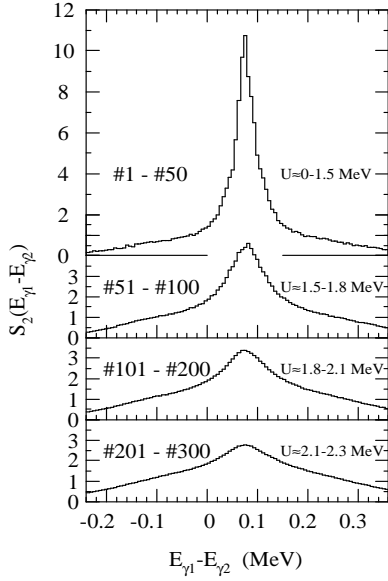


Figure 12: Excitation energy dependence of the two-gamma strength distribution  $S_2(E_{\gamma_1} - E_{\gamma_2})$  for the energy bins covering the first to 50-th, 51-st to 100-th, 101-st to 200-th, and 201-st to 300-th lowest levels at each  $I^\pi$ . The strength is averaged over spin interval  $I = 30 - 51$ .

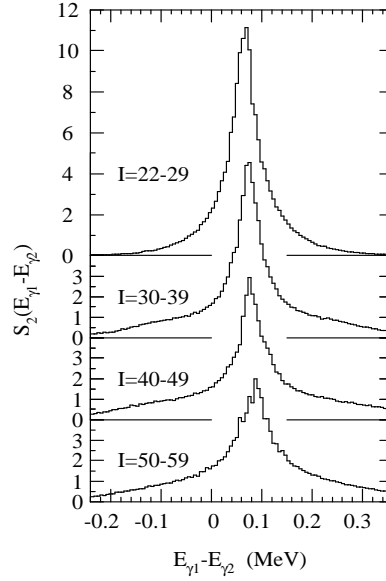


Figure 13: Spin dependence of the two-gamma strength distribution  $S_2(E_{\gamma_1} - E_{\gamma_2})$  for the energy bin covering the lowest 100 levels at each  $I^\pi$ . The strength distribution is shown for different spin intervals;  $I = 22 - 29, 30 - 39, 40 - 49, 50 - 59$ .

### 3.5 Near-yrast rotational bands

The main aim of the present model is to describe the internally excited states and the rotational damping phenomena in the warm region of the spectrum at very high spin. However, it is interesting to study how the two-body residual interaction affects the rotational bands near the yrast line as compared to the standard cranked mean-field calculations which are often used to describe those states.

The calculated and observed rotational bands are compared in Figure 14. The rotational bands below spin  $I \sim 20$  are not reproduced well in the present model. This is because the present calculation does not give a satisfactory description of the pairing correlations, which are important for the rotational bands at low spins. Pairing correlations may also account for the slightly lower moments of inertia of the experimental bands in the angular momentum region around  $I \sim 20$  to 40. This is taken into account by using a reference moment of inertia in Fig.14, which is chosen smaller by about 10% for the experimental bands than for the theoretical ones. In the higher spin region with  $I \gtrsim 30$ , the model reproduces fairly well the overall features of the lowest few bands near the yrast line; above the crossing at  $I \sim 25$ , the  $(-, 1)_1$  band becomes the yrast band, leaving the  $(+, 0)_1$  as the second lowest, both in the theory and in the experiment. The dominant configuration in the  $(-, 1)_1$  band is neutron 1p1h excitation  $(\nu[521]1/2)^1(\nu[642]5/2)^{-1}$  relative to the reference configuration (the  $(+, 0)$  band marked with R in Fig.14). The third lowest  $((+), (0))$  band in the experiments seems to correspond to the  $(+, 0)_2$  bands in the model, whose dominant configuration is the neutron excitation  $(\nu[521]1/2)^2(\nu[642]5/2)^{-2}$ . Furthermore, both the model and the experiment show the band crossings at  $I \sim 40$ . In the calculation, the crossings involve the aligned proton orbits  $\pi h_{9/2}$  and/or  $\pi i_{13/2}$  (See Fig.1). They are, however, slightly sharper than those in the observed bands. This discrepancy also may be attributed to the insufficient pairing correlation in the present calculation (Note that Ref.[37] discusses the smoothness of the crossing in connection with the proton pairing).

In order to show the effects of the interaction, we compare in Fig.14 with the unperturbed

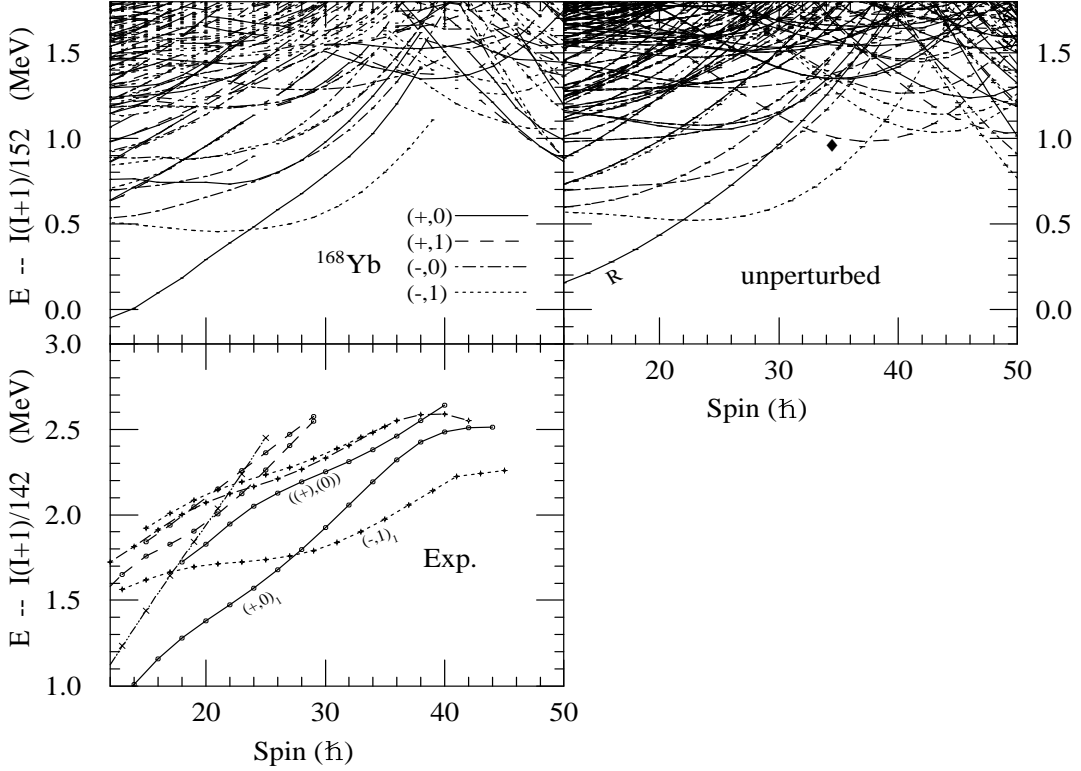


Figure 14: The rotational band structures near yrast line in  $^{168}\text{Yb}$ . The calculated band structure is shown in the left-top panel in a similar way to Fig.4 subtracting the reference rotational energy  $I(I + 1)/152$  MeV. The right-top panel shows the unperturbed rotational bands calculated without the residual two-body force. See text for marks. The left-bottom panel shows the observed rotational bands subtracting the reference energy  $I(I + 1)/142$  MeV [37, 38].

rotational bands which are obtained without the residual interaction. It is noticed that the  $(+, 0)$  configuration taken as the reference (marked with R) gains energy due to the correlation caused by the residual interaction, which includes a part of the pairing effect. On the other hand, the  $(+, 1)$  unperturbed rotational band marked with a diamond is pushed up by the residual interaction. This band has configuration  $(\nu[521]1/2)^1(\nu[642]5/2)^{-1}$  for neutrons and  $(\pi h_{9/2})^1(\pi[411]1/2)^{-1}$  for protons with respect to the reference. Since the neutron and the proton configurations have different spatial density distribution (oblate and prolate along the symmetry axis, respectively), the residual SDI force makes this configuration energetically unfavored. The residual interaction gives, at least in this case, an overall improvement of the description of the near-yrast rotational bands compared to the unperturbed rotational bands with pure independent particle configuration.

## 4 Residual interactions

### 4.1 Interaction strength

Since the rotational damping is controlled predominantly by the configuration mixing caused by the residual interaction, it is interesting to examine the dependence on the two-body residual force. It is also noticed that there is some ambiguity in the strength of the SDI (the literature value ranges as  $V_0 \sim 20/A - 30/A$  MeV, see Appendix B). To examine the dependence of the results on the SDI strength, we performed calculations with various SDI strengths ( $V_0 = 14/A, 20/A, 35/A, 50/A$  MeV). We also check how the results depend on the specific features of the SDI that emphasize the interaction at the nuclear surface and give large matrix elements for the single-particle orbits near

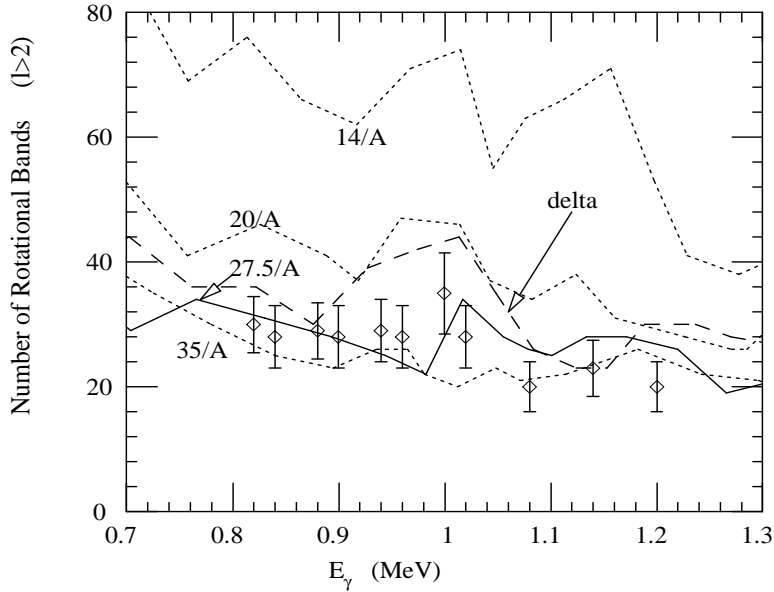


Figure 15: Number of rotational bands calculated with various SDI strengths and with the delta force. The definition of the number of bands is based on the criterion that  $n_{branch} < 2$  for at least 2 steps.

the Fermi surface. For that purpose, we also perform a calculation with a *volume* delta force

$$v(1, 2) = -v_{\delta}\delta(\vec{x}_1 - \vec{x}_2) \quad (31)$$

which does not have the surface effects. For the strength of the volume delta interaction, we used  $v_{\delta,nn} = v_{\delta,pp} = 340 \text{ fm}^3\text{MeV}$  and  $v_{\delta,pn} = 500 \text{ fm}^3\text{MeV}$  taken from Ref.[44], which are evaluated from comparison with more realistic residual interactions, independently of the SDI strength.

Figure 15 compares results from these forces with respect to the number of rotational bands taken as an measure of the onset of rotational damping. The calculated number of bands is rather stable for reasonable values  $20/A - 35/A$  MeV of the SDI strength (See Appendix B), in fairly good agreement with the experimental effective number of path. The volume delta force also gives similar results.

In contrast, if the SDI strength is reduced, e.g., to  $V_0 = 14/A$  MeV, the number of bands increases significantly and overestimates the experimental data. This is because the configuration mixing effects is reduced accordingly (e.g.  $n_{mixing}$  becomes about factor four smaller than with  $V_0 = 27.5/A$  MeV) and the weakened configuration mixing is less capable of causing the rotational damping. On the other hand, the number of rotational bands does not decrease very much increasing the SDI strength. This feature is qualitatively explained by the role of the level densities for the onset of damping. According to Ref.[2], the onset energy  $U_0$  scales with the interaction strength  $v$  only in powers  $U_0 \sim v^{-2/3}$  while the number of levels (or number of rotational bands) below  $U_0$  depends on  $U_0$  in an exponential manner  $exp\sqrt{2aU_0}$  as estimated from the Fermi gas level density. It should be remarked, however, that the rotational band structure near yrast line is significantly deviated from the unperturbed rotational bands (corresponding to the conventional cranking calculations) if the strength exceeds more than  $35/A$  MeV. Such large strength may not be very realistic for the description of low-lying rotational bands near the yrast even though the onset of rotational damping is described fairly well.

## 4.2 Role of high multipole components

In addition to just the strength of the residual interaction, also the spatial properties will affect its ability to generate configuration mixing. Earlier [21] we have shown that a pure pairing plus quadrupole-quadrupole (P+QQ) interaction produces transition strength distributions and level

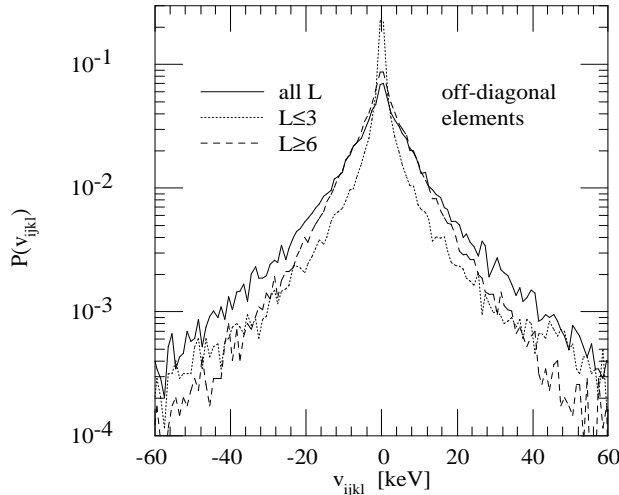


Figure 16: Distribution of the off-diagonal two-body matrix elements  $v_{ijkl}$  of SDI with  $V_0 = 27.5/A$  MeV, binned within intervals of width 1 keV. The angular momentum chosen for the figure is  $I = 40, 41$ . The distribution for the low-multipole part ( $L \leq 3$ ) and for the high-multipole part ( $L \geq 6$ ) of the same SDI are also shown. The latter two have essentially the same r.m.s. value.

spacing distributions which are very different from those generated by the SDI. The P+QQ force provides a good description of only the large matrix elements which lead to collective properties of low-lying levels. It is to be noticed however that the low multipole forces such as P+QQ usually have strong selectivity or selection rules with respect to the Nilsson asymptotic quantum numbers. Contrary, the components with high multipolarity may not have such large matrix elements nor cause the collective effects while they may have less selectivity.

Figure 16 shows the distribution of off-diagonal two-body matrix elements between all possible two particle transitions ( $ij \leftrightarrow kl$ ) conserving parity and signature associated with the interaction matrix elements  $\langle \mu | V_{\text{res}} | \mu' \rangle$  between the basis configurations  $\{ |\mu \rangle \}$ . The selectivity of the low multipole part ( $L \leq 3$ ) of the SDI manifests itself as a surplus of very weak matrix elements, and also of very strong matrix elements. The restriction to very large multipoles ( $L \geq 6$ ) is seen to lead to a more smooth distribution. To investigate how such a selectivity affects the configuration mixing, we perform several calculations in which only the high or the low multipole components of the SDI are taken into account. Low multipole components include  $L \leq 2, 3, 4, 5$  in Eq.(B.3) with the SDI strength  $V_0 = 27.5/A$  MeV, and high multipoles with  $L \geq 3, 4, 5, 6$ . Another calculation has also been done using the P+QQ interaction with the monopole pairing strength  $G_0 = 20/A$  MeV, the quadrupole pairing strength  $G_2 = 2.4\chi_{\text{self}}$  which is estimated from the multipole decomposition of the delta force [45], and the QQ interaction strength  $\chi_{nn} = \chi_{pp} = 0.7\chi_{\text{self}}, \chi_{np} = 3.3\chi_{\text{self}}$  estimated from the selfconsistency condition [40] both for isoscalar and isovector components. A calculation

	r.m.s. (keV)		r.m.s. (keV)
all $L$	19.8		
$L \leq 2$	11.3	$L \geq 3$	16.5
$L \leq 3$	12.3	$L \geq 4$	15.7
$L \leq 4$	16.3	$L \geq 5$	13.4
$L \leq 5$	16.8	$L \geq 6$	12.3

Table 1: The root mean square value  $\sqrt{\langle v_{ijkl}^2 \rangle}$  of off-diagonal matrix elements of the residual two-body force for various multipole decompositions of SDI with  $V_0 = 27.5/A$  MeV. The angular momentum chosen for the table is  $I = 40, 41$ .

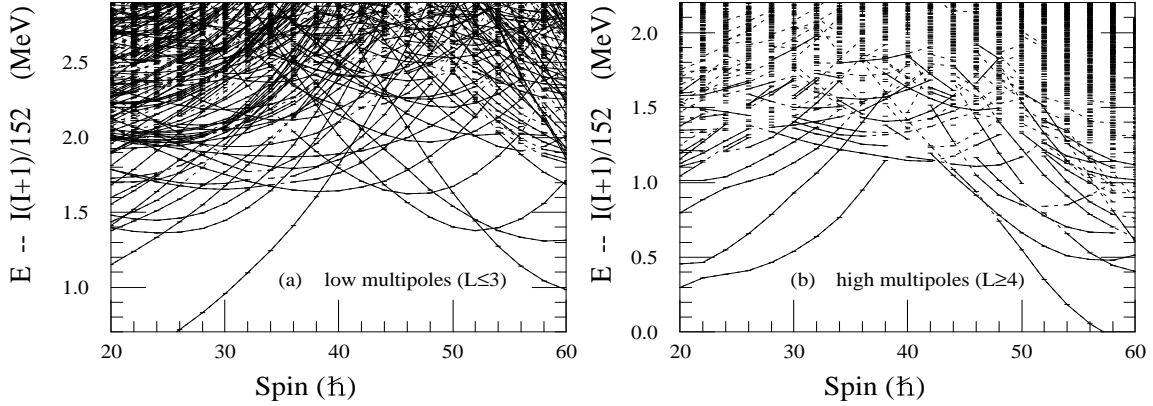


Figure 17: The energy levels and rotational band structure for  $^{168}\text{Yb} (+,0)$  calculated with only (a) the low multipole including  $L \leq 3$  terms of SDI in Eq.(B.3) and (b) the high multipoles  $L \geq 4$ . The strength of SDI is  $V_0 = 27.5/A$  MeV. See Fig.4 for definition of solid and dashed lines.

with the P+QQ interaction with doubled strength is also performed. To show the average size of the two-body matrix elements, the root mean square (r.m.s.) value of the off-diagonal elements is listed in Table 1. Note that the r.m.s. value associated with the P+QQ is 12.7 keV so that it becomes larger than the r.m.s. of the full SDI when the force strength is doubled.

The influence of the different multipolarity on the onset of rotational damping is evident in Fig.17, in which the rotational band structures are displayed in the same way as Fig.4 for the calculation with low multipoles  $L \leq 3$  of SDI as well as for the one with complementary high multipoles  $L \geq 4$ . With the low multipole part, most of the states shown in the figure form a large number of rotational band structures characterized by sequences of strong E2 transitions, apparently different from the calculation Fig.4 with full SDI. On the contrary, the calculation with the higher multipoles of the SDI gives essentially the same behavior as the full SDI except details of individual levels.

To give a more detailed analysis, the number of bands is calculated for various choices of multipoles and plotted in Fig.18. It is noticeable that the low multipoles with  $L \leq 3$  of SDI as well as the P+QQ interaction produce several hundreds of rotational bands, which is much larger than the full multipole SDI and apparently disagree with the experimental data. On the other hand, the high multipoles with  $L \geq 4, 5$  components give essentially the same number of rotational bands as the full multipole SDI. These results point to that the onset of rotational damping essentially originates from the high multipole components  $L \gtrsim 4$  of the two-body residual interaction and the lower multipole components  $L \lesssim 3$  contribute little. It should be noted that the P+QQ with doubled strength gives still too large number of bands while it has larger r.m.s. value of matrix elements than the full multipole SDI. The low multipoles  $L \leq 3$  and the high multipoles  $L \geq 6$  have the same value of r.m.s. while the predicted onset of rotational damping is completely different.

The origin of this difference can be traced back to the distributions of the two-body matrix elements shown in Fig.16, where the distribution of off-diagonal two-body matrix elements  $v_{ijkl}$  is plotted for the SDI with all the multipoles, with the low multipoles containing  $L \leq 3$ , and with the high multipoles  $L \geq 6$  (The same plot for the P+QQ is given in Ref.[21]). The latter two have about the same r.m.s. value of about 12 keV (cf. Table 1). All the three interactions have a distribution which is sharply peaked at  $v_{ijkl} = 0$  as compared to the Gaussian distribution (inverse parabola curve) which is expected in a random limit. In particular, the distribution of the low multipole interaction is significantly concentrated at small values  $|v_{ijkl}| \lesssim$  a few keV, indicating strong selectivity for the matrix elements of the low multipole interaction while the high multipole part of the SDI as well as the full SDI has more uniform distribution, On the other hand, the value of  $P(v_{ijkl})$  for the low multipole part ( $L \leq 3$ ) of SDI is factor 2-3 smaller than for the high multipole part ( $L \geq 6$ ) or the full SDI at around the average strength ( $v \sim 10 - 20$  keV) of the matrix elements. This implies that the basis  $np-nh$  configurations  $\{|\mu\rangle\}$  have less chances to interact with each other via the low-multipole parts of SDI than via the high-multipole parts. In fact, we find that the mixing number  $n_{mixing}$ , Eq.(26), calculated with the low multipole part ( $L \leq 3$ ) of

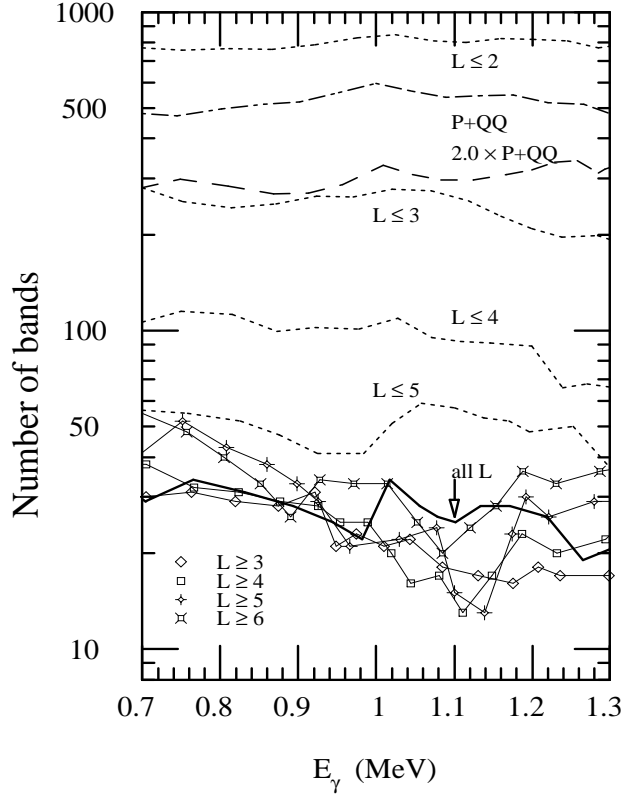


Figure 18: The number of rotational bands for various multipole decompositions of SDI plotted as a function of average gamma-ray energy (See text for details). The definition of the number of bands is the same as in Fig.15. The number of bands calculated with the P+QQ force is also plotted with dotted-dashed line. The result for the P+QQ with doubled force strength is plotted with dashed line.

SDI is significantly smaller than those obtained with full SDI or the high multipole part ( $L \geq 6$ ). For example, the average value of  $n_{mixing}$  calculated at  $I^\pi = 50^+$  is around 3 even at  $U \sim 1.5$  MeV, and many of the states around this energy keep a rather pure configuration with  $n_{mixing} \lesssim 2$  (cf.  $\langle n_{mixing} \rangle \sim 10$  and  $\sim 8$  for the full SDI and the high multipole parts  $L \geq 6$ , respectively). Accordingly, one finds that the discrete rotational bands extend to a much higher excitation energy when only the low-multipole parts of SDI are included.

One may consider several reasons for the distribution of the two-body matrix elements being much sharper than the Gaussian. The Gaussian distribution could be obtained if the wave functions of single-particle orbits had no specific structures and were randomly distributed, while such a random situation is not satisfied for the actual cranked single-particle orbits under consideration since the cranked single-particle orbits keep some characteristic structures even in the presence of the deformation and the cranking terms in the mean-field Hamiltonian. As an example of such structures, one could consider angular momentum components of single-particle orbits. Many of the cranked single-particle orbits can be classified as deformation aligned or rotation aligned, depending on whether the angular momentum vector points to the deformation axis ( $z$  axis) or the rotation axis ( $x$  axis), respectively. The deformation aligned orbitals, which correspond to the almost straight lines with small slope in Fig.1, generally carry large and fairly pure  $K$  values (projection of angular momentum along  $z$  axis). The rotation aligned orbitals corresponding to straight lines with large slope are dominated by the components with large total angular momentum  $J$  (e.g.  $i_{13/2}$  for neutrons,  $h_{11/2}, h_{9/2}$ , and  $i_{13/2}$  for protons). These approximate quantum numbers may give rise to strong selectivity in the two-body matrix elements. This effect is expected to be stronger for low multipole interactions than for those containing high multipole contributions. If the angular quantum numbers  $K$  and  $J$  of the single-particle orbits are good quantum numbers and the two-body interaction with

multipolarity  $L$  is considered, there is a selection rule for the  $K$  and  $J$  of the interacting two particles such as  $|K_1 - K_2| \leq L$  and  $|J_1 \pm J_2| \leq L$ . This selection becomes effective for  $L$  which is smaller than the average  $J$  of single-particle orbits near the Fermi surface.

## 5 Conclusions

We have presented results of shell model calculations for rapidly rotating warm nuclei. The model describes microscopically levels and stretched E2 transitions up to a few MeV above yrast at high spin region  $I \gtrsim 20$ . From the numerical calculation for  $^{168}\text{Yb}$ , it is predicted that the rotational damping sets in around  $U \gtrsim 0.8$  MeV above the yrast line. The levels near the yrast line form rotational band structures and the number of the rotational bands is calculated to be around 30 at a given rotational frequency, agreeing with the experimental data extracted from the fluctuation analysis of  $E_\gamma \times E_\gamma$  spectra.

The model predicts some novel features of the rotational damping. The onset of rotational damping takes place quite gradually as a function of internal excitation energy and it shows large fluctuations depending on individual states. The transition region extends from 0.8 MeV to 2 MeV above the yrast line. Even in the region  $U \sim 0.8 - 1.5$  MeV, there remain scars of discrete rotational band structures, which are characterized by short sequences of strong E2 transitions. In keeping with these results, the corresponding strength function associated with two-fold E2 rotational transitions is expected to display a two-component profile with a narrow component generated by strong and correlated transitions surviving in the region of the rotational damping and a wide component whose width is related to the rotational damping width. The origin of rotational damping can be traced back to the high-multipole components ( $L \gtrsim 4$ ) of the residual two-body force acting among the unperturbed cranked shell model states.

The overall aim of the present work has been to extend the cranked mean field to finite temperatures, including an effective two-body force which is capable of coupling many-particle many-hole excitations built upon the cranked mean field. The main advantage of the model is the inclusion of all excitations of the independent particle motion up to around 2 MeV above yrast line, and this implies a realistic behavior of the level density. As a drawback, the truncation of the shell model space adopted in the present paper does not allow for surface vibrations and pair-correlated states to be generated. However, since the effective two-body force applied includes terms which generate such correlations, it would be an interesting future subject to extend the shell model space and to study whether the shell model approach is able to describe also the correlated states at high spins.

## Acknowledgment

We deeply acknowledge fruitful and stimulating discussions with B. Herskind, A. Bracco, and S. Leoni. We also thank S. Frauendorf and Y.R. Shimizu for providing us the cranked Nilsson and the liquid drop codes, respectively. One of the author, M.M., acknowledges the Danish Research Council as well as the INFN for support of his stay at Niels Bohr Institute and INFN Sez. Milano where a part of the research reported here was carried out.

## Appendix A. Diabatic cranked Nilsson single-particle basis

The adiabatic basis or the eigen solutions of the cranked Nilsson Hamiltonian sometimes show abrupt changes in the routhian energy  $\{e'_i(\omega)\}$  and wave functions  $\{\psi_i(\omega)\}$  when the rotational frequency is varied. This is caused by the “repulsive interaction” associated with crossings among two orbits



with the same quantum numbers. The diabatic single-particle basis can be constructed by removing the unwanted repulsion at each of the crossings.

First, we need to specify the unwanted crossings which cause the abrupt changes in the adiabatic basis. In order to measure the abruptness, it is necessary to give a relevant scale for the changes in the rotational frequency. Since the rotational band structure associated with the collective rotation is concerned, we consider the change in the frequency corresponding to the angular momentum change  $\Delta I = 2$  of two unit. Namely, we examine the change in  $\{e'_i(\omega)\}$  and  $\{\psi_i(\omega)\}$  against the variation from  $\omega_I$  to  $\omega_{I+2}$ , where  $\omega_I$  is the rotational frequency corresponding to a given angular momentum  $I$  (See, sect.2.2). The relation between  $\omega$  and  $I$  approximately follows  $I \sim J\omega$ ,  $J$  being the moment of inertia.

Now the unwanted crossings are specified by the following three criteria. i) The single-particle wave functions at  $\omega_I$  and  $\omega_{I+2}$  should not be very different for the diabatic basis. Given an orbit  $i$  at  $\omega_I$ , an overlap condition

$$|\langle \psi_i(\omega_I) | \psi_j(\omega_{I+2}) \rangle| > \Omega_{thr} \quad (\text{A.1})$$

is checked for orbits  $j$  at  $\omega_{I+2}$ . If there is no orbits satisfying this condition, we consider the orbit  $i$  as interacting at  $\omega_I$ . ii) The single-particle contribution to the dynamic moment of inertia  $j_i^{(2)} = -d^2 e'_i / d\omega^2 = dj_{x,i} / d\omega$  is calculated at  $\omega_I$ . If its absolute magnitude exceeds a threshold  $j_{thr}$ , the orbit  $i$  is considered as interacting at  $\omega_I$  since the moment of inertia for the configurations involving this orbit deviates significantly from the other configurations. iii) Under the assumption that only two diabatic levels interact simultaneously with a constant interaction, all the features of the level repulsion are specified by the interaction strength  $v_{int}$ , the crossing frequency  $\omega_{crs}$  and another quantity  $\delta$  which is the relative energy shift of diabatic levels under the change  $\omega_I \rightarrow \omega_{I+2}$  in the rotational frequency. A measure of the abruptness of the crossing is given by a dimensionless parameter  $v_{int}/\delta$  [30]. For small  $v_{int}/\delta$ , below a threshold  $e_{thr}$ , the adiabatic basis shows an abrupt change near the crossing point. Here the interaction strength  $v_{int}$  and the crossing frequency  $\omega_{crs}$  are extracted by searching the frequency where the distance  $|e'_1(\omega) - e'_2(\omega)|$  between the interacting orbit pair is minimum. The interaction strength  $v_{int}$  is a half of the minimum distance. The parameter  $\delta$  is expressed in terms of the diabatic energies of the interacting orbits, i.e.,

$$\delta = 1/2 \{ e'_{\text{dia},i}(\omega_I) - e'_{\text{dia},i+1}(\omega_I) - (e'_{\text{dia},i}(\omega_{I+2}) - e'_{\text{dia},i+1}(\omega_{I+2})) \} \quad (\text{A.2})$$

where the expression for the diabatic energy is given by (A.5). The conditions i) and iii) are essentially the same as those introduced by Bengtsson [30].

The three criteria discussed above represent similar conditions about the abruptness, and are not mutually independent. In practice, we first pick up candidates with use of the first two criteria, and then examine them in terms of the third criterion in order to finally determine the pairs of orbits for which the diabatic basis should be constructed. A reasonable choice of the thresholds is found to be  $\Omega_{thr} = 0.933$ ,  $j_{thr} = 20 \text{ MeV}^{-1}$  and  $e_{thr} = 1.8$ .

Once the unwanted crossings are specified, we then remove the interaction among the two crossing orbits. In doing this, we assume that the crossings are isolated and that each crossing is represented by a two-level model with a constant interaction strength [46]. For the two-level model, the relation between the adiabatic and the diabatic basis is analytically expressed. The routhian and the wave function of the diabatic basis are expressed as

$$e'_{\text{dia},1 \text{ or } 2} = \pm \sqrt{(e'_1 - e'_2)/2^2 - v_{int}^2} + (e'_1 + e'_2)/2 \quad (\text{A.3})$$

$$\psi_{\text{dia},1} = \cos(\theta)\psi_1 - \sin(\theta)\psi_2 \quad (\text{A.4})$$

$$\psi_{\text{dia},2} = \sin(\theta)\psi_1 + \cos(\theta)\psi_2 \quad (\text{A.5})$$

with

$$\cos(\theta) = \sqrt{\left(1 + \frac{e'_{\text{dia},1} - e'_{\text{dia},2}}{e'_1 - e'_2}\right)} / 2 \quad (\text{A.6})$$

in terms of the eigensolutions of the cranked Nilsson single-particle Hamiltonian, which form the adiabatic base. This prescription is applied to the interacting orbit pairs within a frequency interval

between  $\omega_{min}$  and  $\omega_{max}$ , at which the distance between the interacting adiabatic orbits becomes 10 times the interaction strength  $v_{int}$ . There is only small difference between the diabatic and adiabatic basis outside of this frequency interval, where the latter should be used.

## Appendix B. Surface Delta Interaction

The cranked Nilsson single-particle basis is expanded in the harmonic oscillator basis  $\varphi_{nljm}(r_t\theta_t\phi_t) = R_{nl}(r_t)\varphi_{ljm}^{angle}(\theta_t\phi_t)$  in the single-stretched polar coordinate system  $\{r_t\theta_t\phi_t\}$  where the single-stretch means the scaling  $x_i = \sqrt{\omega_0/\omega_i}x'_i$  with the anisotropic oscillator frequencies of the Nilsson potential. Correspondingly, the SDI can be expressed in terms of the stretched coordinates

$$v(1,2) = -V'\delta(\vec{x}'_1 - \vec{x}'_2)\delta(r_t - R) \quad (\text{B.1})$$

$$= -V'\frac{\delta(r_{t,1} - R)}{r_{t,1}}\frac{\delta(r_{t,2} - R)}{r_{t,2}}\delta(\Omega_{t,12}) \quad (\text{B.2})$$

where  $\delta(\Omega_{t,12})$  is the delta function for the angle variables. As it is usually prescribed, the radial matrix elements of the SDI interaction is replaced by a constant. Then the SDI interaction acting on the angular and spin wave function  $\varphi_{ljm}^{angle}$  is given

$$v(1,2)^{angle} = -4\pi V_0 \sum_{LM} Y_{LM}^*(\theta_{t,1}\phi_{t,1})Y_{LM}(\theta_{t,2}\phi_{t,2}) \quad (\text{B.3})$$

The evaluation of the angular matrix elements of the spherical harmonics is straightforward [47]. The matrix elements in the cranked Nilsson orbits are then calculated directly.

The interaction strength  $V_0$  is directly related to the strength  $G_0$  of the standard monopole pairing force [20], for which the value around  $20/A - 30/A$  MeV is often used. The requirement of the selfconsistency between induced mean-field and density gives an estimate  $V_0 = 20/A$  MeV [35]. From fits in light nuclei ( $A \lesssim 70$ ), it is estimated that  $V_0 \sim 25/A$  MeV [47]. The analysis of the low-lying collective vibrations and the pairing in rare-earth deformed nuclei gives  $V_0 = 27.5 \pm 6.5/A$  MeV [35]. Thus, we adopt  $V_0 = 27.5/A$  MeV as a representative strength of SDI.

## References

- [1] G.A. Leander, Phys. Rev. **C25** (1982) 2780.
- [2] B.Lauritzen, T.Døssing and R.A.Brogli, Nucl. Phys. **A457**(1986) 61;  
R.A. Broglia, T. Døssing, B. Lauritzen and B.R. Mottelson, Phys. Rev. Lett. **58** (1987) 326.
- [3] J.C.Bacelar, G.B.Hagemann, B.Herskind, B.Lauritzen, A.Holm, J.C.Lisle,P.O.Tjøm, Phys. Rev. Lett. **55**(1985) 1858.
- [4] J.E.Draper, E.L.Dines, M.A.Deleplanque, R.M.Diamond, and F.S.Stephens, Phys. Rev. Lett. **56**(1986)309.
- [5] F.S.Stephens, J.E.Draper, J.L.Egido, J.C.Bacelar, E.M.Beck, M.A.Deleplanque, and R.M.Diamond, Phys. Rev. Lett. **57**(1986)2912;  
F.S.Stephens, J.E.Draper, J.C.Bacelar, E.M.Beck, M.A.Deleplanque, and R.M.Diamond, Phys. Rev. Lett. **58**(1987)2186;  
F.S.Stephens, J.E.Draper, M.A.Deleplanque, R.M.Diamond, and A.O. Macchiavelli, Phys. Rev. Lett. **60**(1988)2129.

- [6] B.Herskind, A.Bracco, R.A.Brogli, T.Døssing, A.Ikeda, S.Leoni, J.Lisle, M.Matsuo, and E.Vigezzi, Phys. Rev. Lett. **68**(1992) 3008.
- [7] T. Døssing, B. Herskind, S. Leoni, M. Matsuo, A. Bracco, R.A. Broglia, and Vigezzi, Phys. Rep. **268** (1996) 1.
- [8] B.Herskind, T.Døssing, S.Leoni, M.Matsuo, and E.Vigezzi, Prog. Part. Nucl. Phys. Vol.28 (Pergamon 1992) p.235;  
B. Herskind, S. Leoni, T. Døssing, G. B. Hagemann, P. Bosetti, A. Bracco, S. Frattini, E. Vigezzi and M. Matsuo, Acta Phys. Pol. **B26** (1995) 153.
- [9] B. Herskind, T. Døssing, D. Jerrestam, K. Schiffer, S. Leoni, J. Lislie, R. Chapman, F. Khazaie and J.N. Mo, Phys. Lett. **B276** (1992) 4;  
B. Herskind, T. Døssing, S. Leoni, M. Matsuo, N. Nica., D.C. Radford and P. Rasmussen, Nucl. Phys. **A557** (1993) 191c.
- [10] B. Herskind, T. Døssing, P. Rasmussen, S. Leoni, A. Bracco, R.A.Brogli, P.Bosetti, E.Vigezzi, M.Matsuo, preprint
- [11] S. Leoni, B. Herskind, T. Døssing, P. Rasmussen, P. Bosetti, A. Bracco, R. Broglia, S. Frattini, M. Matsuo, N. Nica, E. Vigezzi, A. Ataç, M. Bergström, A. Brockstedt, H. Carlsson, P. Ekström, F. Ingebretsen, H.J. Jensen, J. Jongman, G.B. Hagemann, R.M. Lieder, T. Lönnroth, A. Maj, B. Million, A. Nordlund, J. Nyberg, M. Piiparinen, H. Ryde, M. Sugawara, P.O. Tjøm, and A. Virtanen, Nucl. Phys. **A587** (1995) 513.
- [12] T.Guhr and H.A. Weidenmüller, Ann. Phys. **193** (1989) 489.
- [13] J.L.Egido and A. Faessler, Z.Phys. **A339**(1991) 115.
- [14] S.Åberg, H.Flocard, W.Nazarewicz, Ann. Rev. Nucl. Part. Sci., 40(1990)439
- [15] Z.Szymanski, *Fast Nuclear Rotation* (Clarendon Press, Oxford, 1983)
- [16] M.J.A. de-Voigt, J.Dudek, Z.Szymansky, Rev. Mod. Phys. **55** (1983)949
- [17] R. Bengtsson and S. Frauendorf, Nucl. Phys. **A314** (1979) 27; **A327** (1979) 137.
- [18] T.Bengtsson and I.Ragnarsson, Nucl. Phys. **A436**(1985) 14.
- [19] S.Åberg, Phys. Rev. Lett. **64**(1990) 3119;  
S.Åberg, Prog. Part. Nucl. Phys. vol.28 (Pergamon 1992) p.11.
- [20] I. M. Green and S. A. Moszkowski, Phys. Rev. **139** (1965)B790;  
R.Arview and S.A.Moszkowski, Phys. Rev. **145** (1966)830.
- [21] M. Matsuo, T. Døssing, E. Vigezzi and R.A. Broglia, Phys. Rev. Lett. **70** (1993) 2694.
- [22] M. Matsuo, T. Døssing, B. Herskind, S. Frauendorf, E. Vigezzi and R.A. Broglia, Nucl. Phys. **A557** (1993) 211c.
- [23] A.T.Kruppa, K.F.Pal, N.Rowley, Phys. Rev. **C52**(1995)1818.
- [24] T.Mizusaki, T.Otsuka, and P.von Brentano, Nucl. Phys. **A598**(1996) 47.
- [25] J.D.Garrett, *Nuclear Structure 1985* (Elsevier Science, 1985) p.111, ed. R.Brogli, G.B.Hagemann and B.Herskind
- [26] Y.R.Shimizu, J.D.Garrett, R.A.Brogli, M.Gallardo and E.Vigezzi, Rev. Mod. Phys. **61**(1989)131.
- [27] Y.R.Shimizu, Nucl.Phys. **A520**(1990) 477c.

- [28] S.G. Nilsson, C.F. Tsang, A. Sobiczewski, Z. Szymański, S.Wycech, C. Gustafson, I. Lamm, P. Möller, and B. Nilsson, Nucl. Phys. **A131**(1969) 1.
- [29] R.Bengtsson, S.Frauendorf and F.-R.May, Atomic Data and Nuclear Data Tables, **35**(1986) 15.
- [30] T.Bengtsson, Nucl. Phys. **A496** (1989) 56.
- [31] G.Andersson, S.E.Larsson, G.Leander, P.Möller, S.G.Nilsson, R.Bengtsson, Nucl. Phys. **A268** (1976) 205.
- [32] K.Neergård, V.V.Pashkevich, and S.Frauendorf, Nucl. Phys. **A262**(1976) 61.
- [33] S.Åberg, Nucl. Phys. **477** (1988) 18.
- [34] P. Ring and P. Shuck, *The Nuclear Many Body Problem* (Springer-Verlag, 1980).
- [35] A. Faessler, Fortschr. Phys. **16** (1968) 309.
- [36] I.Hamamoto and H.Sagawa, Nucl.Phys. **A327** (1979)99.
- [37] A. Fitzpatrick, S.A. Araddad, R. Chapman, J. Copnell, F. Lind'en, J.C. Lisle, A.G. Smith, J.P. Sweeney, D.M. Thompson, W. Urban and S.J. Warburton, J. Simpson, C.W. Beausang, J.F. Sharpey-Shafer, S.J. Freeman, S. Leoni, and J. Wrzesinski, Nucl. Phys. **A585** (1995)335.
- [38] J.R.B. Oliveira, S. Frauendorf, M.A. Deleplanque, R.M. Diamond, F.S.Stephens, C.W. Beausang, J.E.Draper, C.Duyar, E.Rubel, J.A.Becker, E.A. Henry, and N.Roy, Phys. Rev. **C47**(1993)R926.
- [39] T.R. Werner and J. Dudek, Atomic Data and Nuclear Data Tables, **50**(1992) 179.
- [40] A. Bohr and B.R. Mottelson, *Nuclear Structure*. vol. I (Benjamin, 1969).
- [41] R.A. Broglia, T. Døssing, M. Matsuo, E. Vigezzi, P. Bosetti, A. Bracco, S. Frattini, B. Herskind, S. Leoni, and P. Rasmussen, Zeit. Phys. **A356** (1996) 259.
- [42] A. Bracco, P. Bosetti, S. Frattini, E. Vigezzi, S. Leoni, T. Døssing, Herskind, and M. Matsuo, Phys. Rev. Lett. **76** (1996) 4484;  
E. Vigezzi, S. Frattini, P. Bosetti, A. Bracco, R.A. Broglia, T. Døssing, B. Herskind, S. Leoni, M. Matsuo, Proc. of the Workshop on Heavy Ion Fusion: Exploring the Variety of Nucl. Properties, Padova, 1994, (World Scientific 1995) p.149.
- [43] M. Matsuo, T. Døssing, B. Herskind, S. Frauendorf, Nucl. Phys. **564** (1993) 345.
- [44] B.W. Bush, G.F. Bertsch and B.A. Brown, Phys. Rev. **C45** (1992) 1709.
- [45] I. Hamamoto, Nucl. Phys. **A232**(1974) 445.
- [46] T.Takami, Phys. Rev. Lett. **68** (1992) 3371.
- [47] P.J.Brussard and P.W.M.Glaudemans, *Shell-Model Applications in Nuclear Spectroscopy* (North-Holland, 1977)